

Rare-Earth Molecular Crystals with Ultra-narrow Optical Linewidths for Photonic Quantum Technologies

Diana Serrano¹, Kuppusamy Senthil Kumar^{2,3}, Benoît Heinrich⁴, Olaf Fuhr^{3,5},
David Hunger^{2,6}, Mario Ruben^{2,3,7}, Philippe Goldner¹

¹Chimie ParisTech, PSL University, CNRS, Institut de Recherche de Chimie Paris,
11, rue Pierre et Marie Curie, 75005 Paris, France

²Institute for Quantum Materials and Technologies (IQMT), Karlsruhe Institute
of Technology (KIT), 76344 Eggenstein-Leopoldshafen, Germany

³ Institute of Nanotechnology, Karlsruhe Institute of Technology (KIT),
76344 Eggenstein-Leopoldshafen, Germany

⁴Institut de Physique et Chimie des Matériaux de Strasbourg (IPCMS),
CNRS-Université de Strasbourg, Strasbourg, France

⁵Karlsruhe Nano Micro Facility (KNMF), Karlsruhe Institute of Technology (KIT),

⁶Physikalisches Institut, Karlsruhe Institute of Technology (KIT),
Wolfgang-Gaede Str. 1, 76131 Karlsruhe, Germany

⁷Centre Européen de Sciences Quantiques (CESQ), Institut de Science
et d'Ingénierie Supramoléculaire (ISIS), Université de Strasbourg, France

May 4, 2021

Rare-earth ions are promising solid state systems to build light-matter interfaces at the quantum level. This relies on their potential to show narrow optical homogeneous linewidths or, equivalently, long-lived optical quantum states. In this letter, we report on europium molecular crystals that exhibit linewidths in the 10s of kHz range, orders of magnitude narrower than other

molecular centers. We harness this property to demonstrate efficient optical spin initialization, coherent storage of light using an atomic frequency comb, and optical control of ion-ion interactions towards implementation of quantum gates. These results illustrate the utility of rare-earth molecular crystals as a new platform for photonic quantum technologies that combines highly coherent emitters with the unmatched versatility in composition, structure, and integration capability of molecular materials.

Rare-earth ion (REI)-doped materials are promising systems for optical quantum technologies. At cryogenic temperatures, REIs doped into high quality bulk single crystals, such as Y_2SiO_5 , show exceptionally narrow optical homogeneous linewidths, equivalent to long-lived quantum coherence lifetime (T_2) and suitable for building quantum light-matter interfaces (1). Moreover, REI can present optically addressable electron and/or nuclear spin degrees of freedom that can be leveraged to efficiently store and process quantum information (2, 3). These unique properties in the solid state have been used to demonstrate quantum memories for light (4), light-matter teleportation (5), and frequency and time-multiplexed storage (6). REI-doped crystals are also actively investigated for optical to microwave conversion (7) and quantum processing (8). Besides experiments on high-quality bulk single crystals, strong efforts have recently been launched towards combining REIs with nanophotonic structures (9). This has enabled single REI detection and control (10), fast spontaneous emission modulation (11), lifetime limited single-photon emission (12), and on-chip optical storage (13). Further developments of these exciting topics is, however, impeded by the difficulty to nano-fabricate crystalline host materials that preserve REIs quantum properties for integration into high-quality nanophotonic devices. Molecular chemistry is very attractive in this respect because it offers unmatched flexibility in terms of material composition, fine structural tuning, and integration into photonic structures, as demonstrated by numerous results obtained with single organic molecules embed-

ded in crystalline host lattices (14). However, most organic molecules studied to date lack a spin degree of freedom. Recently, optically addressable molecular spins were demonstrated (15, 16), although with limited optical coherence, hindering their use as coherent spin-photon interfaces. Here, we introduce REI molecular crystals containing trivalent europium that exhibit optical homogeneous linewidths between 5 and 30 kHz, 3 to 4 orders of magnitude narrower than any molecular system (14, 16, 17). This allows us to efficiently exploit the Eu^{3+} nuclear spin degree of freedom by demonstrating $> 95\%$ spin initialization into a single level, and coherent optical storage using atomic frequency combs. We also harness Eu^{3+} narrow optical linewidth to demonstrate ion-ion interactions, which are the basis for high-bandwidth two-qubit quantum gates (8).

The molecular crystal is composed of a mononuclear Eu^{3+} complex $[\text{Eu}(\text{BA})_4](\text{pip})$, where BA and pip stand for benzoylacetate and piperidin-1-ium, respectively (**Fig. 1A**) (18). For clarity, it is referred to as Eu^{3+} complex hereafter. The complex crystallized in $\text{P2}_1/\text{n}$ space group, belonging to the monoclinic crystal system, with crystal lattice composed of anionic $[\text{Eu}(\text{BA})_4]^-$ and cationic piperidin-1-ium units as shown in the supplementary information (**Fig. S1**). The all-oxygen coordination environment around the Eu^{3+} center is best described as a biaugmented trigonal prism with the help of a continuous shape measure calculation (CShM) (19). The point group symmetry around the Eu^{3+} center is assigned to C_{2v} , as inferred from the CShM calculation and luminescence spectrum depicted in **Fig. 1B** (see discussion in SI section 1.1.5). All experiments discussed in the following were performed on crystalline powders with grain sizes of at least 50 nm (see SI section 1.1.4). The Eu^{3+} complex showed high physical and chemical stabilities over time. Repeated cooling cycles had no noticeable effects on optical properties, and no photo-degradation was observed neither at low temperature nor under high laser intensity (**Fig. S8**).

Fig. 1B shows the emission spectrum of the Eu^{3+} complex where the characteristic lines of

trivalent europium are observed (19). We focused on the ${}^7F_0 \rightarrow {}^5D_0$ transition at 580.3778 nm (vacuum) since this transition is associated with narrow linewidths in crystals like Y_2SiO_5 (20). Moreover, it enables optical control of ground state nuclear spins, an important feature for applications in quantum technologies. Transmission experiments revealed a ${}^7F_0 \rightarrow {}^5D_0$ inhomogeneous linewidth (Γ_{inh}) of 6.6 GHz, corresponding to 0.007 nm (**Fig. 1C**). This low value, together with a Lorentzian absorption profile, is typical of high crystalline quality samples with low disorder, and comparable to values obtained in crystals like $Eu^{3+}:Y_2O_3$ (9). Strong absorption was observed in a 500 μm thick powder as a result of the stoichiometric composition of the molecular crystal and light scattering inside the powder. Fluorescence decay experiments led to a lifetime value $T_{1,opt}$ of 540 μs for the 5D_0 level (**Fig. 1D**). This sets a limit of only $1/2\pi T_{1,opt} = 295$ Hz on the optical homogeneous linewidth (Γ_h).

The photon echo (PE) technique, similar to Hahn’s spin echo, enables accurate assessment of narrow homogeneous linewidths (1, 21). Due to its high sensitivity, it can be applied to powders (22), allowing us to measure the optical coherence lifetime, or quantum state lifetime T_2 , of the ${}^5D_0 \leftrightarrow {}^7F_0$ transition in the Eu^{3+} complex (**Fig. 2A**). $\Gamma_h = 1/\pi T_2$ was found equal to 30.2 ± 0.2 kHz, remarkably lower than values reported for single molecules (14), transition metal ions (23), and a previously reported Eu^{3+} complex (16), all in the 10s of MHz range. The Eu^{3+} linewidth in the complex is indeed comparable to those measured in some bulk crystals, such as EuP_5O_{14} (24), and in $Eu^{3+}:Y_2O_3$ nanoparticles (9). We further explored line broadening using stimulated photon echoes (or 3-pulse PE) which allows measuring Γ_h over the time scale of the excited state population lifetime $T_{1,opt}$. We observed an increase in homogeneous linewidth with increasing waiting time τ_W (**Fig. 2B**) until about 1 ms where Γ_h plateaued at a value of ≈ 105 kHz. The Γ_h evolution has an s-shape, as already observed in other REI-doped crystals, and was modelled using a sudden-jump spectral diffusion (SD) model, which could indicate interactions with defects or impurities carrying electron spins (25). The limited line broadening

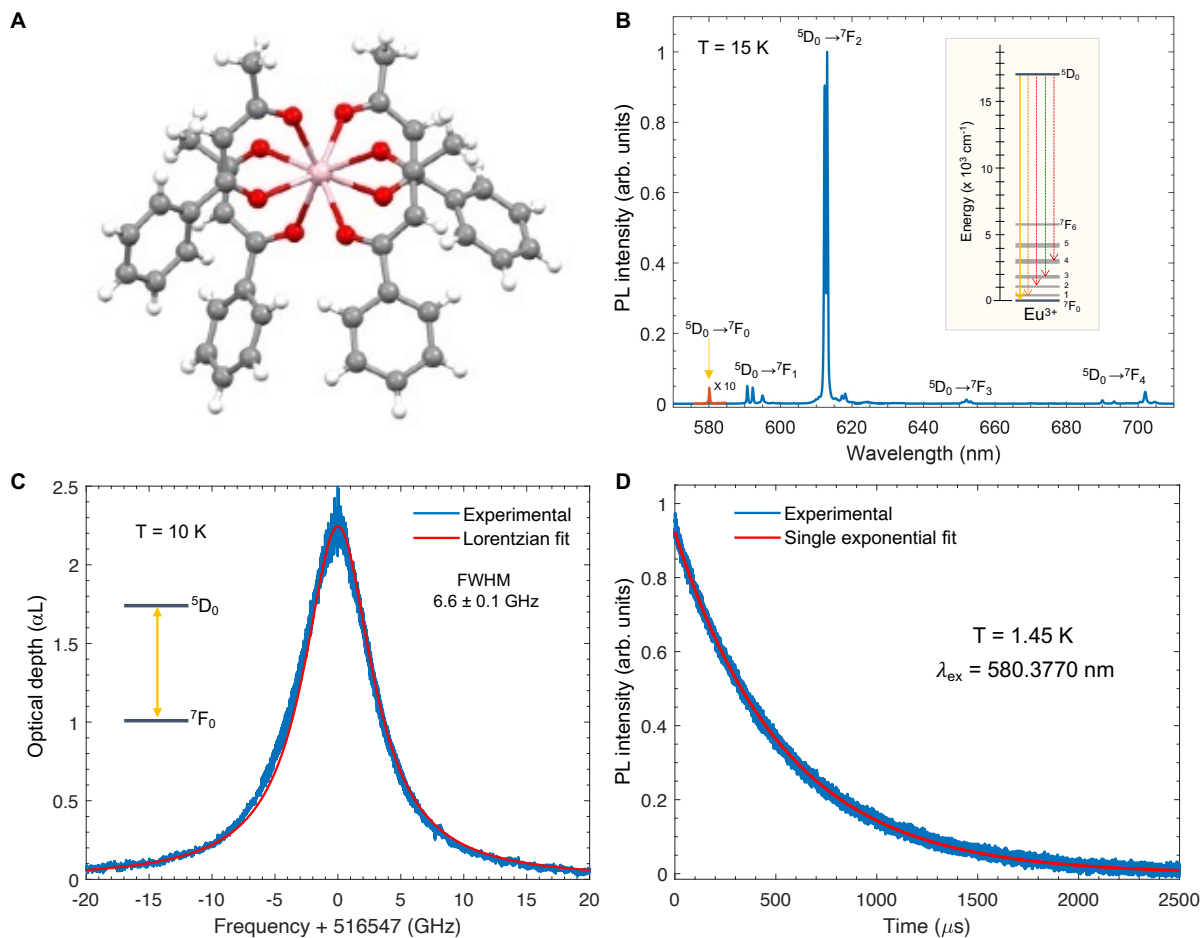


Figure 1: Material and low temperature optical spectroscopy. **A.** X-ray crystal structure of the Eu^{3+} complex. The counter cation is omitted for clarity. Color code: grey, carbon; white, hydrogen; pink, europium; red, oxygen. **B.** Eu^{3+} photo-luminescence (PL) spectrum showing characteristic ${}^5\text{D}_0 \rightarrow {}^7\text{F}_J$ ($J = 0 - 4$) transitions (see inset). All following results were obtained on the ${}^7\text{F}_0 \rightarrow {}^5\text{D}_0$ transition (in red). **C.** ${}^7\text{F}_0 \rightarrow {}^5\text{D}_0$ absorption line recorded on a $500 \mu\text{m}$ thick powder sample. Center wavelength: 580.3778 nm (vacuum). **D.** ${}^5\text{D}_0 \rightarrow {}^7\text{F}_J$ ($J = 1 - 4$) fluorescence decay. Red line: Single exponential fit to data giving a ${}^5\text{D}_0$ population lifetime of $T_{1,\text{opt}} = 540 \mu\text{s}$.

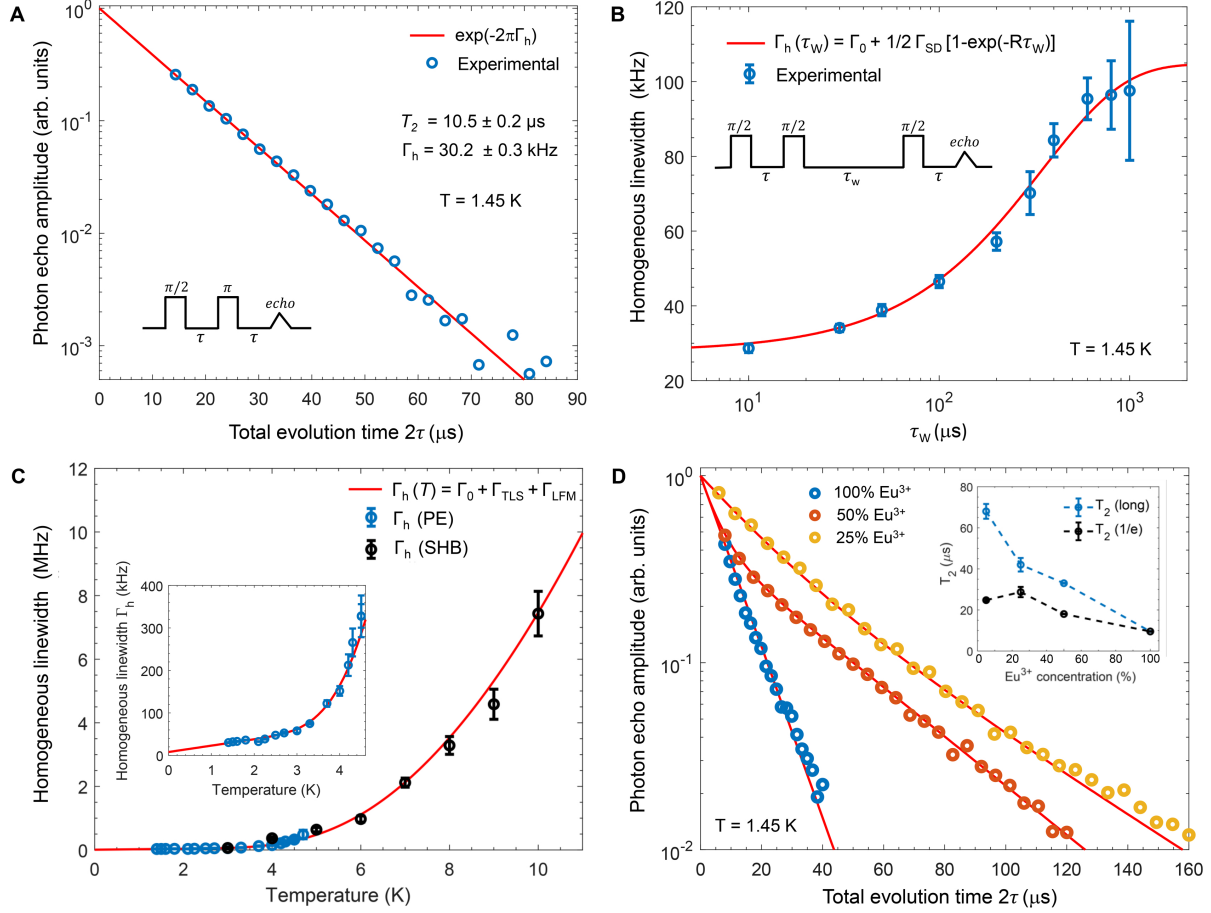


Figure 2: Ultra-narrow optical homogeneous linewidths. **A.** 2-pulse photon echo (PE, pulse sequence shown in inset) decay for the ${}^7F_0 \rightarrow {}^5D_0$ transition. Red line: exponential fit to data giving $T_2 = 10.5 \pm 0.2 \mu\text{s}$ or $\Gamma_h = 1/\pi T_2 = 30.2 \pm 0.2 \text{ kHz}$. **B.** Γ_h as a function of waiting time (τ_w) measured by 3-pulse PE. Red line: fit using a spectral diffusion model yielding a flip rate $R = 2.9 \pm 0.8 \text{ kHz}$ and a width $\Gamma_{SD} = 154 \pm 16 \text{ kHz}$ (see SI section 1.1.7 for more details). **C.** Temperature dependence of Γ_h measured by 2-pulse PE (blue dots) and spectral hole burning (black dots). Red line: fit to a model including contributions from two-level systems (TLS) and quasi-localized low frequency modes (LFMs) (see text and SI 1.1.7). Inset: Zoom on lower temperature range. **D.** PE decays from Y^{3+} -diluted complexes showing T_2 increase with decreasing Eu^{3+} concentration. Red line: single (non diluted crystal) and bi- (diluted crystals) exponential decay fits to data. Inset: $1/e$ echo amplitude decay time T_2 (black dots) and long T_2 component from bi-exponential fits (blue dots) as a function of Eu^{3+} concentration.

over 100s of μs in the Eu^{3+} complex is favorable for spectrally resolved repetitive single ion addressing. Furthermore, lifetime shortening by Purcell enhancement in an optical micro-cavity by a factor of ≈ 100 , would enable generation of indistinguishable single photons (11, 26).

Insights into dephasing mechanisms occurring in the complex were also obtained from the evolution of Γ_h with temperature T , measured by 2-pulse PE and spectral hole burning (SHB) (**Fig. 2C**). Two regimes were identified: for temperatures below 3.5 K, dephasing is dominated by coupling to two-level systems (TLS) and Γ_h increases linearly with T (**Fig. 2C** inset) (27); above 3.5 K, the exponential increase of Γ_h is attributed to quasi-localized low frequency modes (LFMs) (28). Data were modeled using the expression $\Gamma_h(T) = \Gamma_0 + \Gamma_{\text{TLS}} + \Gamma_{\text{LFM}}$, where $\Gamma_{\text{TLS}} = \alpha_{\text{TLS}}T$ and $\Gamma_{\text{LFM}} \approx \alpha_{\text{LFM}} \exp(-\Delta E_{\text{LFM}}/k_B T)$, with k_B the Boltzmann constant. The best fit gave a TLS rate $\alpha_{\text{TLS}} = 15 \pm 5 \text{ kHz K}^{-1}$, as observed in some REI-doped crystals (27), and LFM transition energy $\Delta E_{\text{LFM}} = 580 \text{ GHz}$ (19 cm^{-1}), in the range reported for single molecules (28). The homogeneous linewidth extrapolated to 0 K (Γ_0) is estimated at $8 \pm 4 \text{ kHz}$. This remaining dephasing could be due to Eu^{3+} - Eu^{3+} interactions (20), as the crystal has a high Eu^{3+} concentration, $C_{\text{Eu}} = 9.6 \times 10^{20} \text{ ions cm}^{-3}$. To investigate this effect, an optically inactive REI, Y^{3+} , was introduced in the crystal to reduce C_{Eu} . **Fig. 2D** shows 2-pulse PE decays in a series of diluted crystals. The non-exponential decays suggest distinct populations or environments for the Eu^{3+} ions in these complexes. Increasing coherence lifetimes with decreasing C_{Eu} are observed, especially for the long decay components (**Fig. 2D**, inset), confirming a contribution of Eu^{3+} - Eu^{3+} interactions to dephasing. At the highest dilution investigated here (95% that is 5% Eu^{3+} content), we found a $1/e$ decay time $T_2 = 25 \mu\text{s}$, that is $\Gamma_h = 12.7 \text{ kHz}$. Remarkably, in this sample, photon echoes could be detected even after evolution times of $300 \mu\text{s}$, corresponding to a long decay component of $T_2 = 68 \pm 4 \mu\text{s}$ ($\Gamma_h = 4.6 \pm 0.2 \text{ kHz}$) (**Fig. 2D** inset and SI section 1.1.7). This suggests that synthesis could be optimized to provide a nearly noise-free environment to all Eu^{3+} ions in diluted samples.

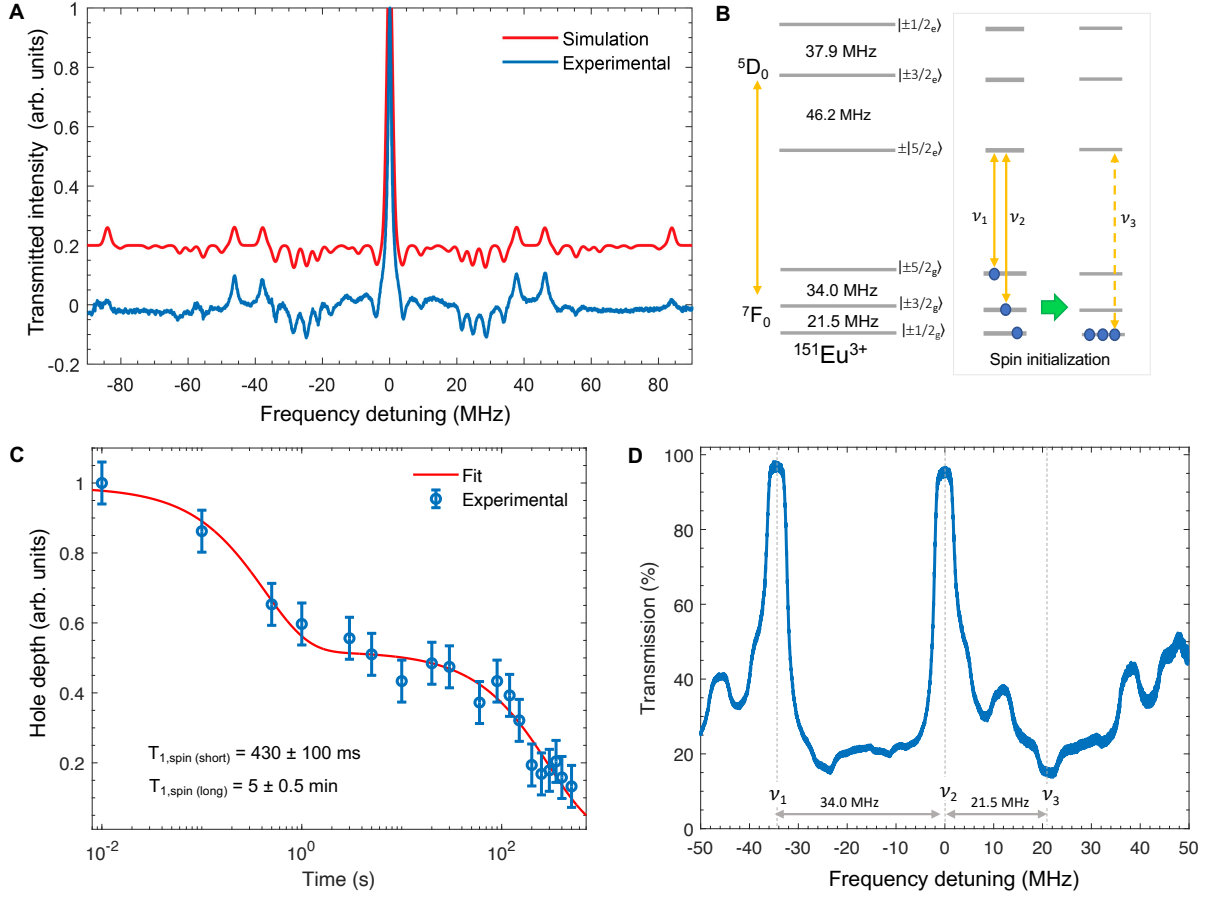


Figure 3: Optically addressable nuclear spins. **A.** Spectral hole burning experimental spectrum of the $^{151}\text{Eu}^{3+}$ complex (blue) compared to simulation (red). **B.** Left - $^{151}\text{Eu}^{3+}$ ground and excited state nuclear spin splittings. Right - Scheme of spin initialization by two-color optical pumping. **C.** Hole decay as a function of delay between burn and readout pulses (see Methods in SI). Red line: double exponential fit yielding spin relaxation times $T_{1,\text{spin}}$ of 430 ± 100 ms and 5.0 ± 0.5 min. **D.** Initialization to a single spin level by two-color optical pumping over a bandwidth of 3 MHz. Applying the pumping scheme shown in B (right), population is transferred from $|\pm 3/2_g\rangle$ and $|\pm 5/2_g\rangle$ levels (deep holes at ν_1 and ν_2), to $|\pm 1/2_g\rangle$ (increased absorption, or anti-hole, at ν_3). Center wavelength 580.3778 nm, $T = 1.45$ K.

Narrow optical linewidths are key to efficiently address REI spins, which enabled detailed investigations of Eu^{3+} nuclear spin states in the complex. First, the nuclear spin structure was determined for the $^5\text{D}_0$ ground state and $^7\text{F}_0$ excited states by SHB in a complex isotopically enriched in $^{151}\text{Eu}^{3+}$. At zero magnetic field, it consists of three doubly-degenerate levels split by quadrupolar interaction (20), giving rise to a complex SHB spectrum after optical pumping. Thanks to the narrow optical linewidth, well-resolved spectral features could be recorded and analyzed (**Fig. 3A**). This allowed us to assign ground and excited state splitting energies (**Fig. 3B-Left**), and transition branching ratios between nuclear spin levels (**Fig. S9**). The same study was done in a natural abundance sample, from which, splitting energies and transition branching ratios were determined for the $^{153}\text{Eu}^{3+}$ isotope (**Fig. S10**). Importantly, the obtained branching ratios show the existence of efficient three-level lambda systems for both isotopes in the Eu^{3+} complex, an important requirement for all-optical spin control (29).

We then probed the dynamics of ground state spin populations by monitoring the spectral hole depth as a function of time delay between burn and readout pulses (**Fig. 3C**). Two distinct decay components can be observed with relaxation times estimated at 430 ± 100 ms and 5.0 ± 0.5 min. This shows that nuclear spin levels can be used as shelving states for at least 100s of ms. Such long times enable efficient optical manipulation of the spin population. As an example, we initialised ions into one nuclear spin level using two-color laser pulses at frequencies ν_1 and ν_2 . This simultaneously depletes the $|\pm 5/2_g\rangle$ and $|\pm 3/2_g\rangle$ ground state spin levels and transfers population into the $|\pm 1/2_g\rangle$ (**Fig. 3B-Right and S11**). As displayed in **Fig. 3D**, nearly full transparency could be induced at ν_1 and ν_2 , which translates to $> 95\%$ spin population into a single level. This also proves that efficient spectral tailoring is possible in the Eu^{3+} complex, an essential feature for many quantum memory and processing protocols based on REIs (4, 8).

We next used the narrow optical linewidths of Eu^{3+} molecular crystals to demonstrate coherent optical storage and controlled ion-ion interactions. In the first case, we used the atomic

frequency comb (AFC) protocol (4) to store a light pulse in the molecular crystal. This protocol enables very low output noise and multiplexed storage, important assets for long distance quantum communications. We first made use of the efficient optical pumping achieved in the Eu^{3+} complex to create an AFC spanning a 6 MHz range, with three 0.9 MHz wide teeth separated by 1.75 MHz (**Fig. 4A**). A storage experiment was then performed with a 0.15 μs long input pulse overlapping the AFC structure. As shown in **Fig. 4B**, the output pulse is observed at a delay $t_s = 0.57 \mu\text{s}$ after the partially transmitted input pulse, in perfect agreement with the teeth spacing since $1/t_s = 1.75 \text{ MHz}$ (4). By varying the teeth spacing and adapting the input pulse length to keep an identical spectral overlap with the comb, output pulses were observed up to about 1 μs storage time, clearly confirming the AFC process (**Fig. 4B** inset). Storage efficiency, defined as the ratio between input and output pulses intensities, was 0.86% for a storage time $t_s = 0.57 \mu\text{s}$, in agreement with theory (see SI section 4). This efficiency could be boosted up to 100% in an optical cavity (30). This could be achieved by crystallizing the Eu^{3+} complex directly on a cavity mirror. Storage times up to several 10s of μs could also be obtained by creating narrower teeth (4) with a suitable laser, given the narrow homogeneous linewidths and limited spectral diffusion in the Eu^{3+} complex.

We finally investigated controlled interactions between Eu^{3+} ions. The scheme we used is based on the difference in permanent electric dipole moments between Eu^{3+} ground (${}^7\text{F}_0$) and excited (${}^5\text{D}_0$) states (31). This difference occurs when Eu^{3+} ions sit in a low symmetry site, which is the case in our molecular crystal (C_{2v} site symmetry). When a control ion is excited, the electric field it produces changes, causing a shift in transition frequency for a nearby target Eu^{3+} ion through the linear Stark effect. This mechanism is the basis for 2-qubit gates and qubit readout in some REI-based quantum computing proposals (8). However, to be useful, ion-ion interactions must be significantly larger than the optical homogeneous linewidth, a condition well matched by our highly-concentrated Eu^{3+} complex with 10 kHz linewidth.

Target and control ions were chosen at different frequencies within the absorption line (**Fig. 1C**) to allow for independent excitation and monitoring. Because of the distribution of distances and orientations and therefore interaction strengths between Eu^{3+} ions, the excitation of control ions results in an additional line broadening Γ_c for target ions, as detailed in SI section 4 (32). Γ_c can be conveniently measured by monitoring the amplitude of a photon echo produced by target ions while an extra pulse excites the control ions.

We first investigated the effect of changing the evolution time (t_{evol}) between control pulse and echo, as shown in **Fig. 4C**. In this case, the echo amplitude varies as $\exp(-\pi\Gamma_c t_{\text{evol}})$ (32). A fit to the experimental data yields $\Gamma_c = 14.5$ kHz, in qualitative agreement with expected $\text{Eu}^{3+}-\text{Eu}^{3+}$ electric dipole interactions (see SI section 4) and previous experiments in non-molecular REI-doped crystals (32). It also provides an upper bound to the ion-ion interaction contribution in the measurements of Γ_h by 2-pulse photon echoes (see SI section 4). We further confirmed this analysis by varying the control pulse intensity I_c . In the weak excitation regime, Γ_c is proportional to the fraction of excited control ions (p), with $p \propto I_c$. We indeed observed the predicted exponential decay of the echo amplitude with increasing p , as displayed in **Fig. 4D**. Finally, the control pulse frequency was varied over several 10s of MHz with fixed t_{evol} and p . No significant change in echo amplitude was observed, ruling out direct light-induced frequency shift of target ions, the so called AC Stark shift (**Fig. 4E**) (13). We therefore conclude that qubit gate and readout schemes based on electric dipole-dipole interactions could be implemented in the molecular crystal. Because of the high Eu^{3+} concentration and narrow linewidth, we estimate that one ion could control thousands of target ions (see SI section 4), a useful property for scaling up REI-based quantum processors (8).

The Eu^{3+} complex investigated in this study is a very promising platform for optical quantum technologies as a robust system with narrow linewidth and long-lived optically addressable spins. Furthermore, significant decrease in optical homogeneous linewidth could be obtained

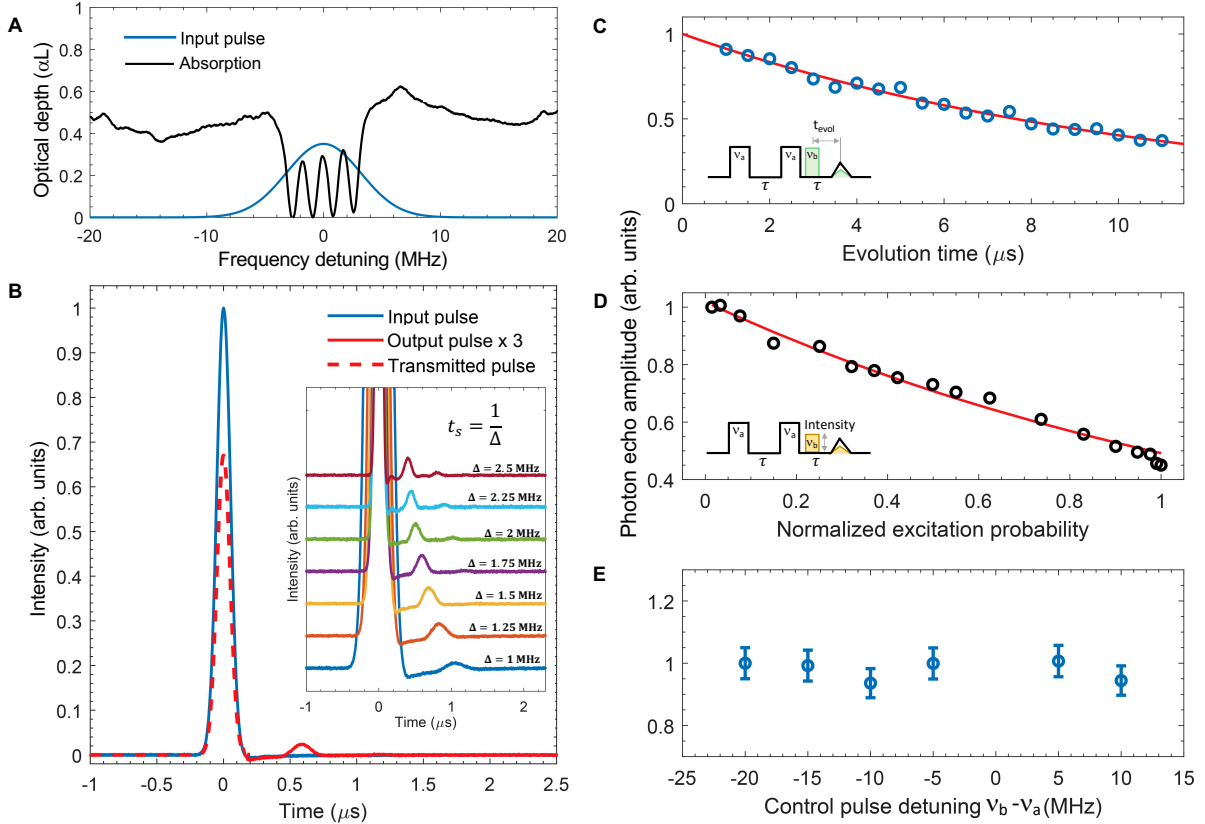


Figure 4: Coherent light storage and optically controlled ion-ion interactions. **A.** Atomic frequency comb (AFC) created by optical pumping within the inhomogeneously broadened ${}^7F_0 \rightarrow {}^5D_0$ line. The 0.9 MHz wide teeth are separated by 1.75 MHz and span 6 MHz. Blue line: Input pulse spectrum. Center wavelength 580.373 nm. **B.** Coherent storage of a $0.15 \mu\text{s}$ long input pulse (blue line) using the AFC structure in **A**. The output pulse appears at $0.57 \mu\text{s}$ (solid red line, intensity $\times 3$) with a storage efficiency of 0.86% (see text). Part of the input pulse is directly transmitted and not stored (dashed line at $0 \mu\text{s}$). Inset: variable storage times t_s obtained by changing AFC teeth frequency separation Δ . Input pulse lengths were adapted to keep identical spectral overlap with AFCs. **C,D,E.** Photon echo amplitude of target ions (at frequency ν_a) as a function of: **(C)** evolution time t_{evol} after excitation of control ions (at $\nu_b = \nu_a - 20 \text{ MHz}$). Red line: exponential fit to data giving a broadening of the target ions linewidth by the control ions of $\Gamma_c = 14.5 \text{ kHz}$ (see text); **(D)** control ions excitation probability (normalized to the maximum value reached experimentally). Red line: exponential fit; **(E)** control pulse detuning. All experiments were performed at 1.45 K.

by lowering temperature, tuning the REI concentration, and optimizing synthesis to decrease residual defects or impurities. In such compounds, interactions with host nuclear spins like ^1H or ^{13}C could become the dominant dephasing mechanisms, which can be reduced using specific isotopes with lower or zero magnetic moments (33). This could also be useful to obtain spin states with long coherence lifetimes, a property that remains to be measured in our samples. The huge possibility in molecular design also opens the way to accurate engineering of the ligand field acting on europium and more generally other REIs of interest for quantum technologies, such as Er^{3+} or Yb^{3+} . This would allow one to optimize transition strengths and frequencies for optimal coupling to light, tune electronic and spin level structures, and coupling to molecular vibrations for long coherence lifetimes. Complexes containing several REIs at close distance can also be synthesized which would enable high-density optically addressable qubit architectures, as shown with REI magnetic molecules in the microwave range (34). Developments towards applications in quantum technologies could greatly benefit from integration of molecular crystals into nanophotonic structures. For example, high-quality and small mode volume optical cavities can dramatically enhance coupling of REI with light, enabling efficient emission from nominally weak transitions (10, 11, 35). This would be facilitated by the broad range of synthesis, functionalization and deposition methods that are available for molecular complexes (14, 33), as well as the scalable production of large amounts of identical molecules. REI molecular crystals could therefore emerge as a highly versatile platform for highly coherent light-matter-spin quantum interfaces for developing applications in quantum communications and processing and fundamental studies in quantum optics.

References

1. P. Goldner, A. Ferrier, O. Guillot-Noël, *Handbook on the Physics and Chemistry of Rare Earths*, J.-C. G. Bünzli, V. K. Pecharsky, eds. (Elsevier, Amsterdam, 2015), vol. 46, pp.

- 1–78.
2. D. D. Awschalom, R. Hanson, J. Wrachtrup, B. B. Zhou, *Nature Photonics* **12**, 516 (2018).
3. M. Zhong, *et al.*, *Nature* **517**, 177 (2015).
4. H. de Riedmatten, M. Afzelius, M. U. Staudt, C. Simon, N. Gisin, *Nature* **456**, 773 (2008).
5. F. Bussi eres, *et al.*, *Nature Photonics* **8**, 775 (2014).
6. A. Seri, *et al.*, *Physical Review Letters* **123**, 080502 (2019).
7. J. G. Bartholomew, *et al.*, *Nature Communications* **11**, 3266 (2020).
8. A. Kinos, *et al.*, *arXiv:2103.15743 [quant-ph]* (2021).
9. T. Zhong, P. Goldner, *Nanophotonics* **8**, 2003 (2019).
10. S. Chen, M. Raha, C. M. Phenicie, S. Ourari, J. D. Thompson, *Science* **370**, 592 (2020).
11. B. Casabone, *et al.*, *arXiv:2001.08532 quant-ph* (2020).
12. T. Zhong, *et al.*, *Physical Review Letters* **121**, 183603 (2018).
13. T. Zhong, *et al.*, *Science* **357**, 1392 (2017).
14. C. Toninelli, *et al.*, *arXiv:2011.05059 [quant-ph]* (2020).
15. S. L. Bayliss, *et al.*, *Science* **370**, 1309 (2020).
16. K. S. Kumar, *et al.*, *Nature Communications* **12**, 2152 (2021).
17. J. Zirkelbach, *et al.*, *Physical Review Letters* **125**, 103603 (2020).
18. L. R. Melby, N. J. Rose, E. Abramson, J. C. Caris, *Journal of the American Chemical Society* **86**, 5117 (1964).

19. K. Binnemans, *Coordination Chemistry Reviews* **295**, 1 (2015).
20. F. Könz, *et al.*, *Physical Review B* **68**, 085109 (2003).
21. I. D. Abella, N. A. Kurnit, S. R. Hartmann, *Physical Review* **141**, 391 (1966).
22. A. Perrot, *et al.*, *Physical Review Letters* **111**, 203601 (2013).
23. H. Riesen, *Coordination Chemistry Reviews* **250**, 1737 (2006).
24. R. Shelby, R. M. Macfarlane, *Physical Review Letters* **45**, 1098 (1980).
25. T. Böttger, C. W. Thiel, Y. Sun, R. L. Cone, *Physical Review B* **73**, 075101 (2006).
26. B. Merkel, A. Ulanowski, A. Reiserer, *Physical Review X* **10**, 041025 (2020).
27. G. P. Flinn, *et al.*, *Physical Review B* **49**, 5821 (1994).
28. B. Kozankiewicz, M. Orrit, *Chem. Soc. Rev.* **43**, 1029 (2014).
29. D. Serrano, J. Karlsson, A. Fossati, A. Ferrier, P. Goldner, *Nature Communications* **9**, 2127 (2018).
30. M. Afzelius, C. Simon, *Physical Review A* **82**, 022310 (2010).
31. R. M. Macfarlane, *Journal of Luminescence* **125**, 156 (2007).
32. S. B. Altner, M. Mitsunaga, G. Zumofen, U. P. Wild, *Physical Review Letters* **76**, 1747 (1996).
33. W. Wernsdorfer, M. Ruben, *Advanced Materials* **31**, 1806687 (2019).
34. C. Godfrin, *et al.*, *Physical Review Letters* **119**, 187702 (2017).
35. J. M. Kindem, *et al.*, *Nature* **580**, 1 (2020).

Acknowledgments

We thank Mikael Afzelius for useful discussions. This project has received funding from the European Union's Horizon 2020 research and innovation programme under grant agreements No 820391 (SQUARE) and the ANR UltraNanoSpec projects, grant ANR-20-CE09-0022 of the French Agence Nationale de la Recherche.

Authors contributions

P. G., M. R. and D. H. conceived and supervised the project. D. S. and K. S. K. were involved in the conceptual development of the project. K.S.K. and M.R. were responsible for the synthesis and characterisation of the isotopologue complexes. B. H. performed powder X-ray diffraction studies and indexed the patterns. O. F. solved the X-ray structure of the complex. D. S. and P. G. performed the optical experiments and analyzed the results. D. S. and P. G. wrote the manuscript with inputs from all authors.

Supplementary materials

Supplementary references are given within brackets. The complete list with details can be found at the end of the document. References in parenthesis refer to the main text.

1.1 Materials and Methods

1-phenylbutane-1,3-dione (99%), Piperidine (99%), and $\text{EuCl}_3 \cdot 6\text{H}_2\text{O}$ (99.9%, trace metal basis) were purchased from Sigma-Aldrich and used as received. $^{151}\text{Eu}_2\text{O}_3$ ($\sim 96\%$ enriched) was purchased from Neonest AB and BuyIsotope, Stockholm, Sweden.

1.1.1 Preparation of the crystalline powder form of the complex

The Eu^{3+} complex studied is a laser chelate reported in the 1960s [1]. We have selected the complex, because it can be prepared from a one-pot reaction, using the commercially available reagents. This allowed us to prepare a series of yttrium-diluted versions and an isotopically ($^{151}\text{Eu}^{3+}$) enriched version of the complex. The complex is stable and can be stored under ambient conditions.

The europium complex discussed in this study was prepared by employing a slightly modified procedure reported by Melby et al. (18). In a typical procedure, 1-phenylbutane-1,3-dione, hereafter referred to as ligand, (1.3 g, 8 mmol) was added to 20 ml of ethanol at 75 °C and dissolved by stirring. To the ligand solution, piperidine (0.8 ml, 8 mmol) was added, and the solution was stirred for 15 minutes. To the pale-yellow solution of the deprotonated ligand, $\text{EuCl}_3 \cdot 6\text{H}_2\text{O}$ (732 mg, 4 mmol) dissolved in 10 ml of water was added. After the completion of the addition, heating was switched off, and the reaction mixture was stirred at room temperature for 24 h, yielding a half-white crystalline precipitate of the complex. The precipitated was filtered, washed with 50 ml of ethanol several times, and dried under reduced pressure overnight.

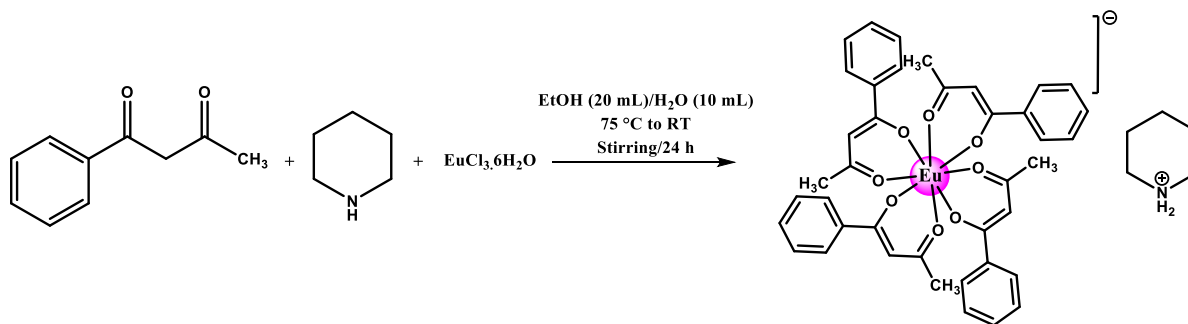


Figure S1: Preparation of the europium complex discussed in this study.

Yield: 0.620 g. Elemental analysis: Calculated for $C_{45}H_{48}EuO_8N$, C, 61.22; H, 5.48; N, 1.59. Found, C, 61.25; H, 5.33; N, 1.77.

A similar procedure was adopted to prepare the yttrium diluted versions of the complex using the appropriate Eu^{3+}/Y^{3+} mole ratio.

Elemental analysis of $C_{45}H_{48}Eu_{0.5}Y_{0.5}O_8N$ (50%-Eu): C, 63.49; H, 5.68; N, 1.65. Found, C, 64.46; H, 5.13; N, 1.58.

Elemental analysis of $C_{45}H_{48}Eu_{0.25}Y_{0.75}O_8N$ (25%-Eu): C, 64.69; H, 5.79; N, 1.68. Found, C, 63.90; H, 5.28; N, 1.66.

Elemental analysis of $C_{45}H_{48}Eu_{0.05}Y_{0.95}O_8N$ (5%-Eu): C, 65.68; H, 5.88; N, 1.70. Found, C, 67.00; H, 5.55; N, 1.74.

1.1.2 Preparation of the $^{151}Eu^{3+}$ -enriched crystalline powder form of the complex

$^{151}EuCl_3 \cdot 6H_2O$ was obtained from $^{151}Eu_2O_3$. In a typical procedure, $^{151}Eu_2O_3$ (200 mg) was dissolved in 10 ml of 1 N HCl by heating at 70 °C for a few minutes. The solution was cooled to RT, and volatiles was removed under reduced pressure. The slurry was dissolved in double-distilled water, and volatiles was removed under reduced pressure. After three such dissolution-evaporation cycles, the solids were dried under reduced pressure overnight, yielding

$^{151}\text{EuCl}_3 \cdot 6\text{H}_2\text{O}$ in a quantitative yield.

Ligand (0.13 g, 0.8 mmol) was added to 2 ml of ethanol at 75 °C and dissolved by stirring. To the ligand solution, piperidine (about 0.08 ml, 0.8 mmol) was added, and the solution was stirred for 15 minutes. To the pale-yellow solution of the deprotonated ligand, $^{151}\text{EuCl}_3 \cdot 6\text{H}_2\text{O}$ (0.074 mg, 0.4 mmol) dissolved in 1 ml of water was added. After the completion of the addition, heating was switched off, and the reaction mixture was stirred at room temperature for 24 h, yielding a half-white crystalline precipitate of the complex. The precipitated was filtered, washed with ethanol several times, and dried under reduced pressure overnight.

Yield: 0.092 g. Elemental analysis: Calculated for $\text{C}_4\text{H}_5\text{N}_8\text{EuO}_8$, C, 61.22; H, 5.48; N, 1.59. Found, C, 62.04; H, 4.865; N, 1.54.

1.1.3 Preparation of X-ray quality crystals of the complex

X-ray crystal structure of the complex reported in the literature was obtained from ethanol, and it was reported that the complex crystallizes in two isomeric forms, α and β , with distinct emission characteristics (2, 3). The $^5\text{D}_0 \rightarrow ^7\text{F}_2$ lines appear at 612.3 nm and 613.05 nm for the α -form and at 611.3 nm and 613.5 nm for the β -form. Since we have used a different solvent system (EtOH- H_2O mixture) to prepare crystalline powder forms of the complex, it is necessary to elucidate the isomeric nature of the complex. Moreover, unambiguous elucidation of the phase purity of the crystalline powders is also necessary, considering the nature of results discussed in the study. Therefore, X-ray quality crystals of the complex were prepared by adopting a slightly modified procedure compared to the one used for the preparation of the crystalline powder form of the complex.

Ligand (1.3 g, 8 mmol) was added to 20 ml of ethanol at 75 °C and dissolved by stirring. To the ligand solution, piperidine (0.8 ml, 8 mmol) was added, and the solution was stirred for 15 minutes. To the pale-yellow solution of the deprotonated ligand, $\text{EuCl}_3 \cdot 6\text{H}_2\text{O}$ (732 mg, 4

mmol) dissolved in 10 ml of water was added. The reaction mixture was stirred at 75 °C for 2 h and filtered when hot. X-ray quality single crystals of the complex were obtained after two days. CCDC 2007594.

Elemental analysis: Calculated for $C_{45}H_{48}EuO_8N$, C, 61.22; H, 5.48; N, 1.59. Found, C, 61.03; H, 5.22; N, 1.74.

High-resolution PL spectra of the crystalline powder form of the complex depicted in the main text revealed the presence of ${}^5D_0 \rightarrow {}^7F_2$ lines at 612.34 nm and 613.05 nm, indicating the presence of α -isomers in the powder form of the complex. The good match between the patterns obtained from the single-crystal X-ray diffraction (SC-XRD) studies and powder X-ray diffraction (PXRD) studies indicate the phase purity of the samples, as discussed below.

1.1.4 Establishment of phase purity of the samples

The phase purity of the crystalline powder samples utilized for optical studies was established by comparing the PXRD patterns of the powders to the pattern simulated from the SC-XRD structure of Eu complex. All complexes gave similar PXRD patterns as they organize in the same type of structure with only tiny shifts in reflection positions due to slight deviations of lattice parameters (**Fig. S2**). The phase purity is confirmed by the absence of additional reflections. For 100%-Eu³⁺ complex, the shape of reflections is slightly broadened and corresponds to average crystalline domain sizes about 50 nm, as evaluated from (10 $\bar{1}$) reflection using Scherrer equation with shape factor $K = 0.9$. The shape is close to the natural beam width for the other samples, meaning that crystallites have average sizes of at least 100 nm or higher.

The molecular self-assembly consists in the arrangement of complexes and counter-ions into layers, whose shifted superposition forms a lamellar structure of one molecular layer periodicity and a monoclinic lattice with $Z = 4$ molecules per cell (**Fig. S3**).

From single-crystal to powder structure, the molecular volume (V/Z) of the Eu³⁺ complex

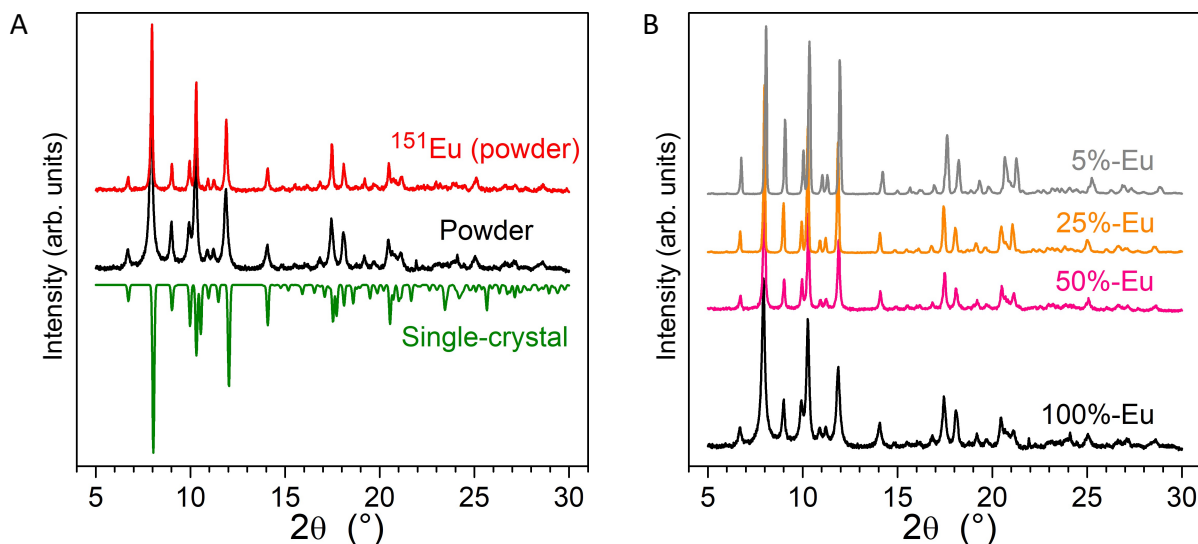


Figure S2: Powder X-ray diffraction (PXRD) patterns of complex series. **A:** PXRD patterns of 100% Eu^{3+} complex (black) and 100% $^{151}\text{Eu}^{3+}$ complex (red) at 293 K, as compared to pattern simulated from single-crystal structure of Eu^{3+} complex at 150 K (inverted trace in green). **B:** PXRD patterns at 293 K of Y^{3+} -diluted Eu^{3+} complex series (pink, orange and grey) compared to 100% Eu^{3+} complex (black).

increases by 3.25% through a balanced expansion of layer thickness d and molecular area (i.e., layer portion area per molecule (A_{mol}), see Table S1). This variation is explainable by the effect of thermal expansion between the different temperatures of measurement — 150 K for SC-XRD and 293 K for PXRD. The structures of Eu^{3+} and $^{151}\text{Eu}^{3+}$ complexes have identical parameters within errors. The Y^{3+} -diluted Eu^{3+} complexes form pure structures with geometrical parameters close to that of neat Eu^{3+} complex. Specifically, the lanthanide substitution leads to slightly higher or slightly lower molecular volumes (+0.7% for 25%-Eu, -2.2% for 5%-Eu) while $(\sqrt{A_{mol}})/d$ ratio hardly varies.

Experimental

The diffraction patterns were obtained with a transmission Guinier-like geometry. A linear focalized monochromatic $\text{CuK}\alpha 1$ beam ($\lambda = 1.54056 \text{ \AA}$) was obtained using a sealed-tube generator (600 W) equipped with a bent quartz monochromator. The samples were filled in

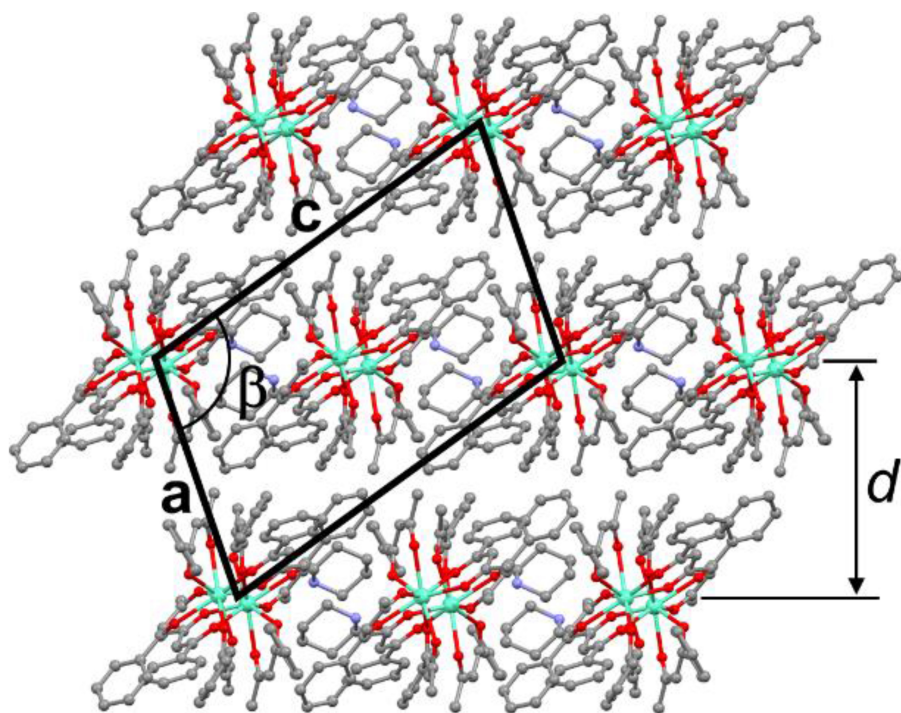


Figure S3: Self-assembly of Eu³⁺ complexes in the single-crystal lattice at 150 K, viewed along b-axis. Anionic Eu³⁺ complexes and piperidinium counter cations are arranged in layers of thickness d , parallel to the $\mathbf{b} \times (\mathbf{a} + \mathbf{c})$ plane of the monoclinic $P2_1/n$ cell.

Method	T(K)	Sample	Lattice parameters ($\text{\AA}, ^\circ$), cell volume V (\AA^3) [$Z = 4$ molecules per lattice] layer spacing $d = d_{10\bar{1}}$ (\AA), molecular area $A_{mol} = (V/Z)/d$ (\AA^2)
SC-XRD	150	Single-crystal	$a = 11.6399, b = 19.5760, c = 18.5229,$ $\alpha = 90, \beta = 107.024, \gamma = 90$ $V = 4035.7, d = 10.983, A_{mol} = 91.86, (\sqrt{A_{mol}})/d = 0.8727$
PRXD	293	100%-Eu ³⁺	$a = 11.918, b = 19.636, c = 18.529,$ $\alpha = 90, \beta = 106.07, \gamma = 90$ $V = 4035.7, d = 10.983, A_{mol} = 91.86, (\sqrt{A_{mol}})/d = 0.8727$
PRXD	293	100%- ¹⁵¹ Eu ³⁺	$a = 11.912, b = 19.638, c = 18.537,$ $\alpha = 90, \beta = 106.11, \gamma = 90$ $V = 4035.7, d = 10.983, A_{mol} = 91.86, (\sqrt{A_{mol}})/d = 0.8727$
PRXD	293	50%-Eu ³⁺	$a = 11.901, b = 19.644, c = 18.503$ $\alpha = 90, \beta = 105.90, \gamma = 90$ $V = 4035.7, d = 10.983, A_{mol} = 91.86, (\sqrt{A_{mol}})/d = 0.8727$

Table S1: Structural parameters of the complex series.

home-made sealed cells of adjustable thickness. Acquisition times were of 24 h or 48 h. The patterns were recorded on image plates and scanned by Amersham Typhoon IP with 25 μm resolution. $I(2\theta)$ profiles were obtained from images, by using a home-developed software.

1.1.5 Point group symmetry around Eu³⁺ in the complex

Reports from the 1960s and 1970s (4,5) and the presence of $^5D_0 \rightarrow ^7F_0$ transition in the photoluminescence (PL) spectrum (19) of the complex indicate that symmetry around Eu³⁺ could be C_{1h} ($n = 1, 2, \text{etc.}$), C_n ($n = 1, 2, \text{etc.}$), C_{nv} ($n = 2, 3, \text{etc.}$), or C_s . However, to the best of our knowledge, a clear assignment of a particular point group symmetry around Eu³⁺ in the complex is yet to be established. To assign the symmetry, we have performed Continuous Shape Measure analysis (CShM) [6] and analysed the high-resolution PL spectrum of the complex (see **Fig. 1B** in the main script). The lowest possible value in the CShM analysis indicates the most plausible coordination geometry; a CShM value of 0.169 indicates the possibility of square antiprism coordination environment with D_{4d} point group around Eu³⁺. However, it is

well established that the ${}^5D_0 \rightarrow {}^7F_0$ induced-electric dipole transition is not allowed in the D_{4d} point group, and the point group symmetry should be lower than D_{4d} . The next lowest values are 2.268, 2.484, and 2.826 corresponding to bi-augmented trigonal prism (C_{2v}), triangular dodecahedron (D_{2d}), and bi-augmented trigonal prism J50 (C_{2v}), respectively. The D_{2d} point group symmetry is ruled out due to the presence of ${}^5D_0 \rightarrow {}^7F_0$ transition. Therefore, it is likely that the point group symmetry around the Eu^{3+} is C_{2v} .

Coordination geometry	Point Group	CShM value
Octagon	D_{8h}	28.599
Heptagonal pyramid	C_{7v}	23.020
Hexagonal bipyramid	D_{6h}	17.600
Cube	O_h	10.369
Square antiprism	D_{4d}	0.169
Triangular dodecahedron	D_{2d}	2.484
Johnson gyrobifastigium J26	D_{2d}	16.713
Johnson elongated triangular bipyramid J14	D_{3h}	27.423
Biaugmented trigonal prism J50	C_{2v}	27.423
Biaugmented trigonal prism	C_{2v}	2.268
Snub diphonoid J84	D_{2d}	5.230
Triakis tetrahedron	T_d	11.136
Elongated trigonal bipyramid	D_{3h}	22.907

Table S2: CShM analysis of Eu^{3+} complex.

Eu^{3+} -center luminescence is used as a spectroscopic probe to elucidate the point group symmetry around the Eu^{3+} . That is, by counting the number of peaks in the PL spectrum of Eu^{3+} complexes, the point group symmetry around Eu^{3+} complexes can be reliably assigned, as discussed by Binnemans (19). The presence of one, three, and four peaks for the ${}^5D_0 \rightarrow {}^7F_0$, ${}^5D_0 \rightarrow {}^7F_1$ and ${}^5D_0 \rightarrow {}^7F_2$ transitions, respectively, confirms that the point group symmetry around Eu^{3+} in the complex is C_{2v} .

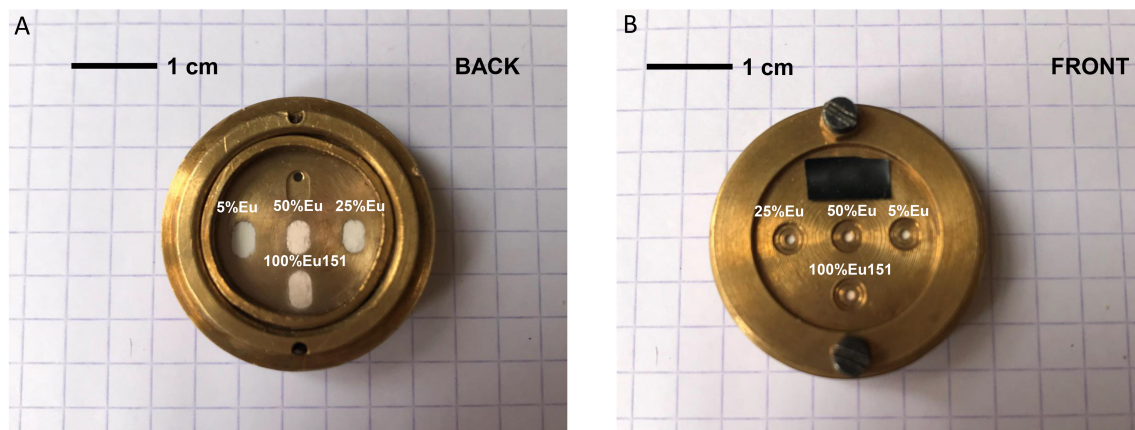


Figure S4: Sample holder. **A.** Back side showing four sample containers filled with crystalline powders of different Eu^{3+} complexes. **B.** Front side of the sample holder. The small openings prevent stray beam (i.e. light not interacting with the powders) to reach the detector.

1.1.6 Optical setups

Optical absorption, photoluminescence (PL) decays, photon echo (PE) and spectral hole burning measurements were performed in a He bath cryostat (Janis SVT-200) under resonant excitation of the ${}^5\text{D}_0 \leftrightarrow {}^7\text{F}_0$ transition of Eu^{3+} . The excitation source was a tunable CW dye laser (Sirah Matisse DS) with ~ 300 kHz linewidth. Temperature-dependent measurements were performed by tuning the He gas pressure ($T < 4$ K) and using a built in resistance as heater ($T > 4$ K). The temperature of the sample holder was monitored with a Si diode (Lakeshore DT-670). Pulse sequences were created using an acousto-optic modulator (AOM - AA Optoelectronic MT200-B100A0, 5-VIS, 200 MHz central frequency), in double pass configuration, driven by an arbitrary waveform generator (Agilent N8242A) with 625 MS s^{-1} sampling rate.

The crystalline powders were filled into a home-built sample holder made of brass. This holder is composed of five individual sample containers which have front and rear optical access through glass windows (**Fig. S4**). Each container was filled with ~ 5 mg of powder forming slabs of about $500 \mu\text{m}$ in thickness. The excitation beam was focused on the containers' front

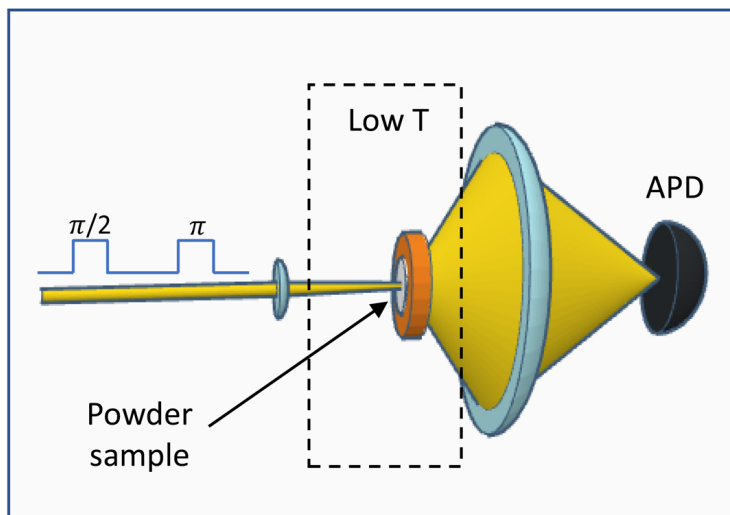


Figure S5: Collection setup. Light scattered by a powder sample within the cryostat is collected by a large-diameter lens and focused on the avalanche photodiode (APD) detector.

openings by a 75-mm-diameter lens placed in front of the cryostat window. Excitation beam and lens were vertically and/or horizontally translated to study one sample after another during measurements. Light scattered by the powders and transmitted through the back openings was collected by a lens sitting outside the cryostat as shown in **Fig. S5**. Signals were detected with avalanche photodiodes (Hamamatsu C5460 with 10 MHz bandwidth for spectral hole burning, and Thorlabs 110 A/M with 50 MHz bandwidth for all other measurements).

1.1.7 Low temperature photoluminescence and optical absorption measurements

Photoluminescence (PL) measurements at 15 K were carried out for the isotopically purified $^{151}\text{Eu}^{3+}$ complex using a closed-cycle cold finger cryostat. The $^5\text{D}_0$ level was resonantly excited at 580.4 nm with a tunable optical parametric oscillator (OPO) pumped by a Nd^{3+} YAG Q-switched laser (Ekspla NT342BSH, 6 ns pulse length and 10 Hz repetition rate). Spectra were recorded using an Acton SP2300 spectrometer equipped with 1200 groove/mm holographic grating and an ICCD camera (Princeton Instruments).

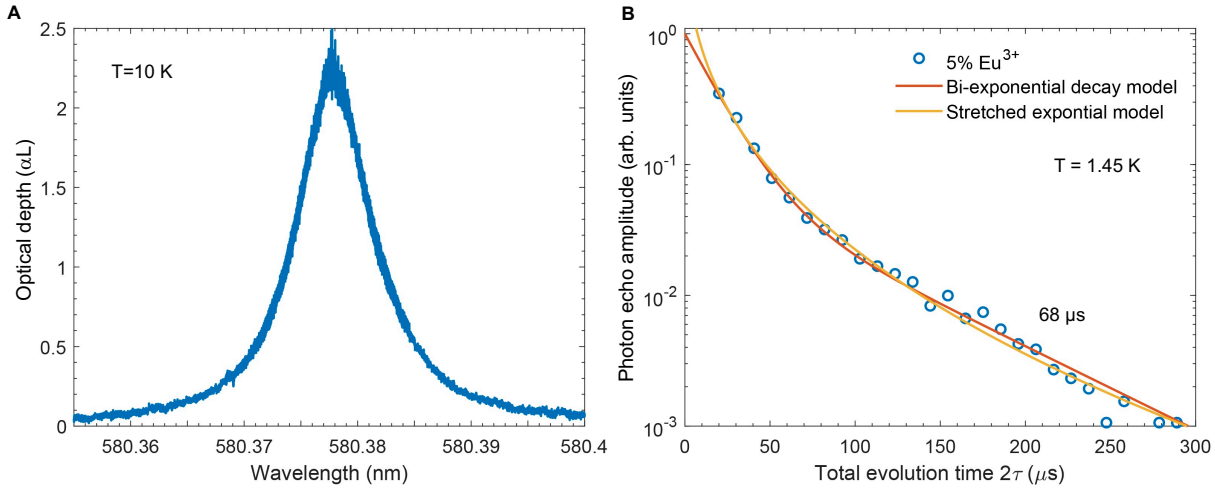


Figure S6: Low temperature high resolution and optical coherence spectroscopy. **A:** Optical absorption as a function of excitation wavelength peaking at 580.3778 nm and presenting a linewidth of 0.007 nm. **B:** 2-pulse photon echo decay from the 5%Eu³⁺-95%Y³⁺ diluted complex showing non exponential character. The decay was fitted with a bi-exponential decay with $T_{2,fast} = 17 \mu s$ and $T_{2,slow} = 68 \mu s$ (red), and a stretched exponential $a \exp(-t^b)$, with $b = 0.388$ (blue).

Optical density (αL) as a function of excitation wavelength (**Fig. S6A**) was measured in transmission mode for the ¹⁵¹Eu³⁺ complex at 1.45 K. αL was calculated as $-\ln(I_{online}/I_{offline})$, with I_{online} and $I_{offline}$, the scattered laser intensities transmitted through the crystalline powder at the optical transition wavelength (online), and in a no-absorption region (offline), respectively (**Fig. S6A**). The inhomogeneous broadening of the transition (Γ_{inh}) was determined by a Lorentzian fit to the absorption curve as a function of frequency (**Fig. 1C**). PL decays were recorded at low temperature for the ¹⁵¹Eu³⁺ complex and Y³⁺-diluted complexes after a single pulse (1-ms long), under resonant excitation of the ⁵D₀ level, yielding comparable decay curves and population lifetimes ($T_{1,opt} \sim 540 \mu s$) for all samples.

1.1.8 Photon echo and spectral hole burning spectroscopic investigations

We detected photon echoes from the Eu³⁺ complexes in form of crystalline powders, which we used to determine the optical coherence lifetime T_2 , and optical homogeneous linewidth

($\Gamma_h = 1/\pi T_2$) for the ${}^5D_0 \leftrightarrow {}^7F_0$ transition. In the 2-pulse sequence, a first pulse ($\pi/2$) creates a coherent superposition between ground and excited states, and a second pulse (π) is applied after some delay (τ), to reverse the phase evolution of the Eu^{3+} -ion ensemble. This results in a collective coherent emission (echo) at time 2τ (**Fig. S7A**). As τ increases, the echo amplitude decreases due to the accumulation of phase shifts induced by perturbations such as vibrations or spin flips occurring in the ions environment, with an echo decay rate proportional to Γ_h .

In addition to 2-pulse photon echoes, we used stimulated echoes to investigate perturbations arising at longer time scales than T_2 , producing homogeneous line broadening by spectral diffusion (SD). In the 3-pulse sequence, the first $\pi/2$ pulse is followed by a second $\pi/2$ pulse so that the phase evolution of the ion ensemble is stopped during a waiting time (τ_W), typically, up to the T_1 time scale. After τ_W , a third and last $\pi/2$ pulse is applied leading to echo emission at time $2\tau + \tau_W$ (**Fig. S7B**). Echo amplitudes from 2-pulse and 3-pulse PE experiments were detected through the fast Fourier transform (FFT) of the beating between the photon echo signal and a frequency-detuned laser pulse (heterodyne pulse, with detuning = 30 MHz). During measurements, the laser wavelength was scanned at 500 MHz s^{-1} to prevent echo signal loss due to spectral hole burning. The length and intensity of the $\pi/2$ and π pulses were optimized to obtain maximum photon echo amplitudes, with typical pulse lengths between 1 and 2 μs , and an input power of 300 mW. A short-pass filter was set in front of the APD detector to reject the strong PL emission in the Eu^{3+} complexes. The echo amplitude obtained by FFT was averaged over 50 sequences to improve signal-to-noise ratio. For single exponential echo decays, the optical coherence lifetime (T_2) was directly derived as $\exp(-2\tau/T_2)$. Diluted complexes presented non-exponential decays which could be described by bi-exponential decay curves and/or stretched exponential curves $\exp(-\tau^b)$ (**Fig. S6B**), where b is the stretching parameter. This non-exponential behavior indicates a distribution of T_2 values in these samples, most likely due to the presence of different environments around the Eu^{3+} centers.

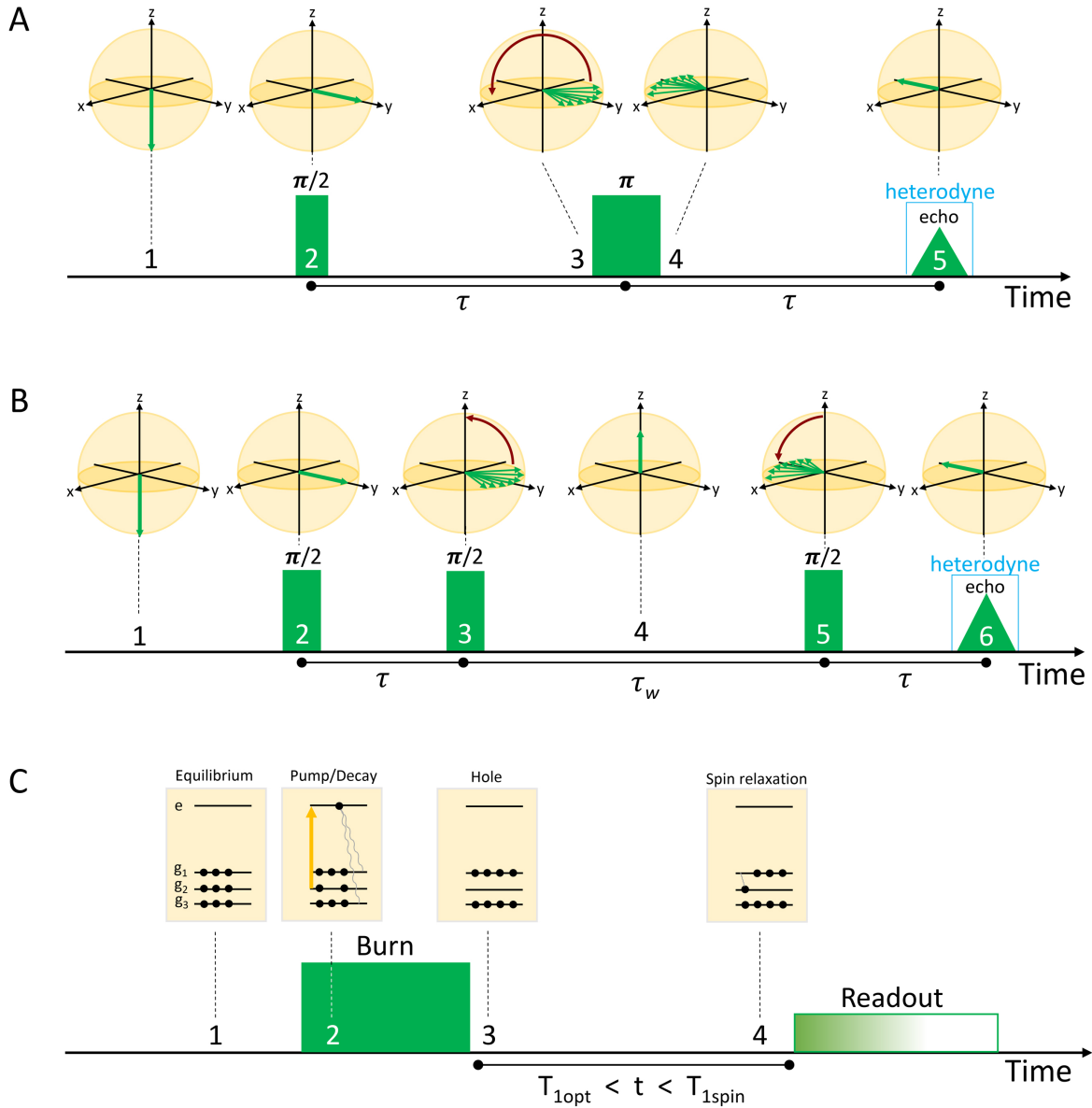


Figure S7: Photon echo (PE) and spectral hole burning (SHB) pulse sequences. **A:** 2-pulse and **B:** 3-pulse photon echo sequences. The phase evolution of the ion ensemble is schematically represented in a Bloch sphere. **C:** Spectral hole burning sequence. The change of the nuclear spin population distribution during and after the burn pulse is schematically represented.

Γ_h as a function of τ_W was modeled by the sudden-jump spectral diffusion (SD) model (25), with $\Gamma_h = \Gamma_0 + 1/2(1 - \exp(-R\tau_W))$. Best-fit parameters yield a flip rate R of 2.9 ± 0.8 kHz and spectral diffusion linewidth contribution at half maximum (Γ_{SD}) of 154 ± 16 kHz. The linewidth at $\tau_w = 0$ (defined as Γ_0 in the model) was found equal to 28 ± 4 kHz, in good agreement with 2-pulse PE results. SD is tentatively attributed from R and Γ_{SD} values to the presence of paramagnetic impurities in the molecular crystals (29).

Spectral hole burning (SHB) spectra from isotopically enriched $^{151}\text{Eu}^{3+}$ and natural abundance complexes, both stoichiometric, were obtained by applying a single pulse, referred to as burn pulse, of 1 ms length and excitation power of 15 mW. After a waiting time of 10 ms, the spectrum was read out with a 2-ms-long scanning pulse with 5 mW input power and 200 MHz scanning range around the burning frequency (**Fig. S7C**). The time before readout was set to 10 ms (i.e. $\gg T_{1,opt}$ to enable spontaneous relaxation from the optical excited state, followed by progressive trapping into non-pumped nuclear spin levels. The SHB spectra were corrected from the AOM frequency-dependent response by dividing by a readout trace obtained with the burn pulse turned off. A series of high-power pulses scanning over 200 MHz was applied at the end of the sequence to reset the ground-state population back to equilibrium. The population lifetime of the ground-state spin levels ($T_{1,spin}$) was determined by monitoring the hole depth as a function of waiting time between burn and readout pulses. The hole decay curve presents two distinct decay rates, estimated by bi-exponential decay fit to the experimental data (**Fig. 3C**).

Spectral holes were measured as a function of temperature up to 10 K, with Γ_h derived from the holewidths (Γ_{hole}) as:

$$\Gamma_h = \Gamma_{hole}/2 - \Gamma_{SD} - \Gamma_{laser} \quad (1)$$

where Γ_{SD} and Γ_{laser} are the spectral diffusion and laser linewidth contributions to the hole width. By comparison to Γ_h obtained from 2-pulse PE experiments, we estimate that Γ_{SD} and

Γ_{laser} add a total contribution of 1.1 MHz to the hole width. This value is indeed larger than the sum of Γ_{SD} obtained from stimulated echoes (153 kHz) and Γ_{laser} (300 kHz), which we attribute to laser instabilities at the 10 ms time scale leading to a larger effective laser linewidth. The temperature-dependent SHB and PE datasets were fitted by:

$$\Gamma_h(T) = \Gamma_0 + \alpha_{\text{TLS}}T + \alpha_{\text{LFM}} \frac{\exp(-\Delta E_{\text{LFM}}/k_B T)}{(1 - \exp(-\Delta E_{\text{LFM}}/k_B T))^2} \quad (2)$$

where Γ_0 is the residual linewidth at 0 K, α_{TLS} expresses the coupling to two-level system (TLS) and α_{LFM} the coupling to low-frequency modes (LFMs), with ΔE_{LFM} the LFM energy and k_B the Boltzmann constant. Best-fit values for these constants are $\alpha_{\text{TLS}} = 15$ kHz and $\alpha_{\text{LFM}}=106$ MHz, $\Gamma_0 = 8$ kHz, and $\Delta E_{\text{LFM}} = 583$ GHz (19 cm^{-1}). We attribute at least part of the residual broadening at zero K to ion-ion interactions producing instantaneous spectral diffusion (ISD). This is motivated by the observed Γ_h reduction when increasing the Eu^{3+} - Eu^{3+} distance in diluted complexes. Moreover, the Eu^{3+} - Eu^{3+} control-target interaction experiment provide an upper bond to the ISD contribution at 14.5 kHz (see section 4 below).

2 Photostability and reproducibility

The photostability of the Eu^{3+} complex was investigated by monitoring the PL intensity of the $^5\text{D}_0$ level of Eu^{3+} under CW excitation of the $^5\text{D}_0 \rightarrow ^7\text{F}_0$ line using the same experimental configuration than in PE and SHB experiments. A long-pass filter, placed in front of the APD detector, was used to reject the excitation wavelength. As shown in **Fig. S8**, the PL remains constant and no sign of photobleaching is observed. Moreover, no evidence of degradation of the crystalline powder was observed after repeated low-temperature experiments under high-power laser intensity.

Reproducibility was assessed by comparing photon echo decays from powder samples produced under equivalent synthesis conditions but belonging to different production batches.

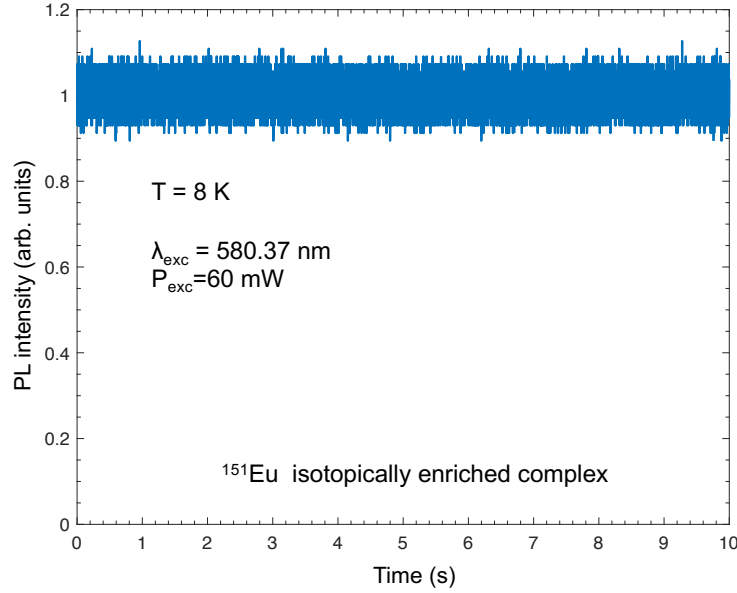


Figure S8: Photostability of the Eu^{3+} complex. $^5\text{D}_0$ PL intensity under CW excitation measured at 8 K for the isotopically enriched complex. The constant PL signal confirms absence of photobleaching in the complex.

Sample to sample T_2 variations were found lower than 10%.

3 $^{151}\text{Eu}^{3+}$ and $^{153}\text{Eu}^{3+}$ nuclear spin structures

The $^5\text{D}_0$ ground state and $^5\text{D}_0$ excited state nuclear spin levels for $^{151}\text{Eu}^{3+}$ and $^{153}\text{Eu}^{3+}$ isotopes were derived from SHB spectra. This was achieved by detailed analysis of the holes and anti-holes frequency positions and depths. As the nuclear spin is $I = 5/2$ for both isotopes, the hyperfine structure consists of three doubly-degenerated levels labelled $\pm 1/2$, $\pm 3/2$ and $\pm 5/2$. SHB spectra from the $^{151}\text{Eu}^{3+}$ complex and a natural abundance complex are given in Figs. **S9** and **S10**, respectively. Nuclear-spin splitting of 21.5 and 34 MHz for the ground state, and 46.2 MHz and 37.9 MHz for the excited state, as well as transition branching ratios, BR_{ij} (**Fig. S9** inset), were obtained by least-square-fitting to the experimental spectrum for the nine possible optical transitions between ground state and excited state nuclear spin levels, where $i =$

$\pm 1/2_g, \pm 3/2_g, \pm 5/2_g$ and $j = \pm 1/2_e, \pm 3/2_e, \pm 5/2_e$, respectively. Since the total transition probability from a particular ground state level i , towards the three excited states j must be 1 ($\sum_i BR_{ij} = 1$), and the same applies for transitions from an excited state j towards the ground states i , ($\sum_j BR_{ij} = 1$), the number of BR_{ij} parameters to be fitted is reduced from nine to four. The simulated spectrum in **(Fig. S9)**, showing very good agreement with the experimental one, was obtained with best-fit BR_{ij} values. Nuclear spin splittings and transition branching ratios for the $^{153}\text{Eu}^{3+}$ isotope were determined from a natural abundance Eu^{3+} complex **(Fig. S10)**, following the same analysis and least-square fitting method. Splittings of 55.7 MHz and 87.3 MHz for the ground state and 118.2 and 96.8 MHz for the excited state were obtained **(Fig. S10)** and BR_{ij} values given in inset in **Fig. S10B**. Despite the complex SHB structure shown by this sample, the simulation shows excellent agreement with the experimental result.

The nuclear spin level ordering for the $^{151}\text{Eu}^{3+}$ isotope could be determined from asymmetries in the SHB spectrum [8]. The complexity of the SHB spectrum in the natural abundance complex prevents this fine analysis, but we can safely assume that the level ordering is the same in the $^{153}\text{Eu}^{3+}$ case than in the $^{151}\text{Eu}^{3+}$ since the hyperfine structure is determined by the quadrupole interaction (see below).

Finally, we calculated spin Hamiltonian parameters for the $^5\text{D}_0$ and $^7\text{F}_0$ levels in the Eu^{3+} complex. The nuclear spin structure of Eu^{3+} at zero magnetic field is described by the quadrupole Hamiltonian (H_Q) [10]:

$$H_Q = P[(I_{z'}^2) - I(I + 1)/3] + (\eta/3)(I_{x'}^2 - I_{y'}^2) \quad (3)$$

with P representing the quadrupole coupling constant, and η the electric field gradient asymmetry parameter. $x'y'z'$ refer here to the principal axes of the electric field gradient tensor. We used the nuclear spin splittings derived from SHB to calculate P and η for the $^7\text{F}_0$ and $^5\text{D}_0$ ground and excited states, for $^{151}\text{Eu}^{3+}$ and $^{153}\text{Eu}^{3+}$ isotopes (Table S3). We note that the

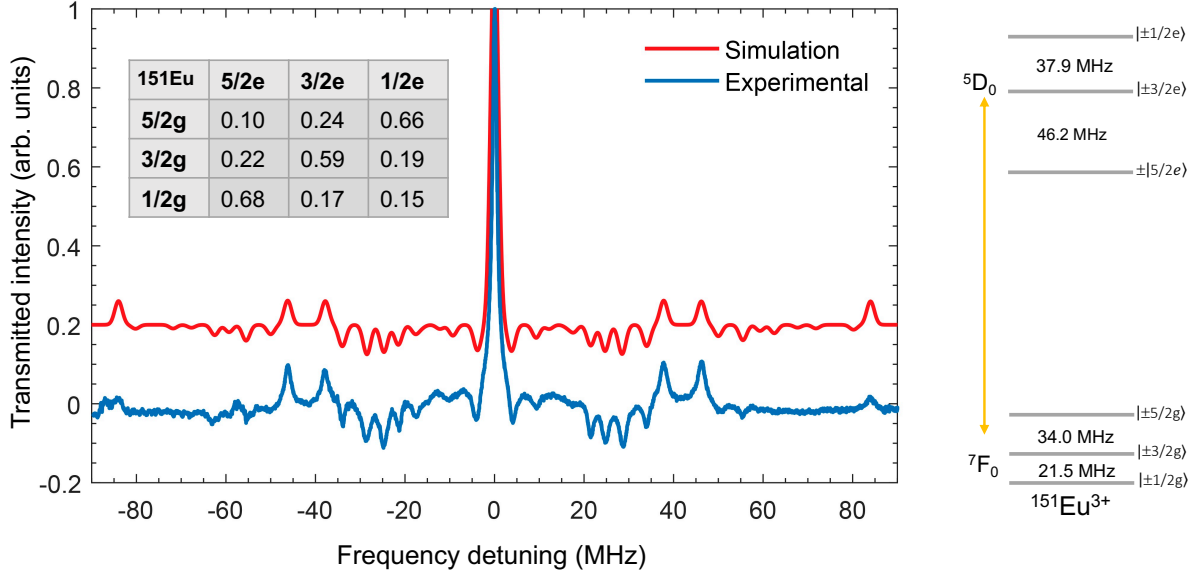


Figure S9: Nuclear spin structure and transition branching ratios for ¹⁵¹Eu³⁺. Experimental and best-fit simulations of the SHB spectrum for the ¹⁵¹Eu³⁺ complex. Inset: transition branching ratio values (BR_{ij}) for ¹⁵¹Eu³⁺.

Level	P	η
¹⁵¹ Eu ³⁺ ground	8.84	0.47
¹⁵¹ Eu ³⁺ excited	-12.6	0.77
¹⁵³ Eu ³⁺ ground	22.73	0.48
¹⁵³ Eu ³⁺ excited	-32.2	0.77

Table S3: Calculated ground-state and excited-state quadrupole Hamiltonian parameters, P and η , for ¹⁵¹Eu³⁺ and ¹⁵³Eu³⁺ isotopes in the Eu³⁺ complex.

P_{153}/P_{151} ratio is equals to 2.57 and 2.56 for the ground and excited states, respectively, comparable to the ratio of the bare quadrupolar coupling constants ($P_{153}/P_{151}=2.55$ [9]). This confirms the almost pure quadrupolar nature of the zero field nuclear spin splittings in the Eu³⁺ complex.

Figure S11 shows the experimental SHB spectrum resulting from > 95% nuclear spin population initialisation to the $|\pm 1/2_g\rangle$ level. This spectrum was obtained by optical pumping at frequencies $\nu_1 = -34$ and $\nu_2 = 0$, with $\nu_2 - \nu_1$ matching the nuclear spin transition frequency between the $|\pm 3/2_g\rangle$ and $|\pm 5/2_g\rangle$ levels. A simulated SHB spectrum is also displayed in

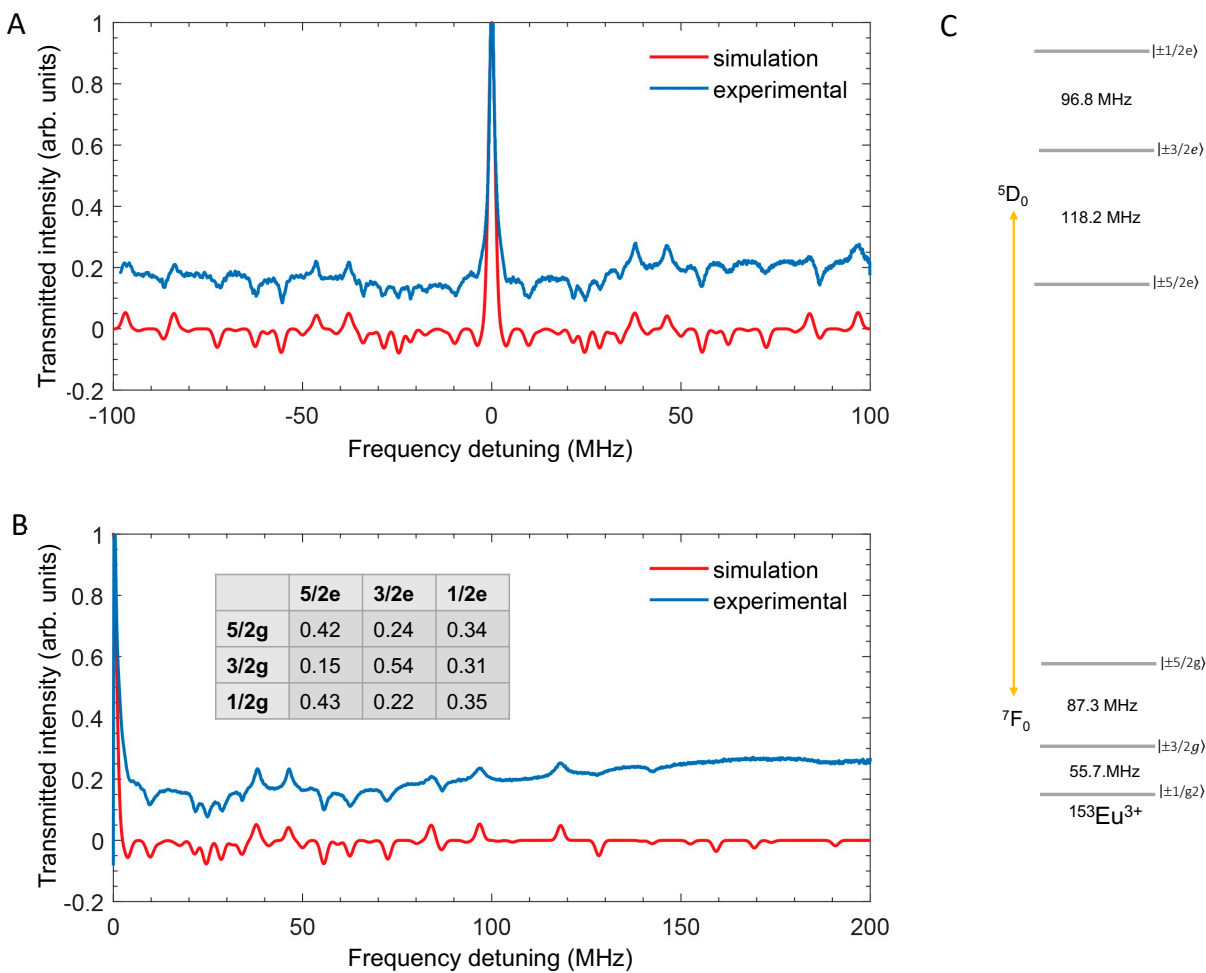


Figure S10: Nuclear spin structure and transition branching ratios for $^{153}\text{Eu}^{3+}$. Experimental and best-fit simulations for the natural abundance Eu^{3+} complex. **A:** SHB spectrum centered on the central hole. **B:** SHB spectrum showing structures in the 0 to 200 MHz frequency detuning region. For detunings > 100 MHz, all observed holes and antiholes are due to the $^{153}\text{Eu}^{3+}$ isotope. **C:** Energy level scheme for $^{153}\text{Eu}^{3+}$ in the complex. Inset: Transition branching ratio values (BR_{ij}) for $^{153}\text{Eu}^{3+}$.

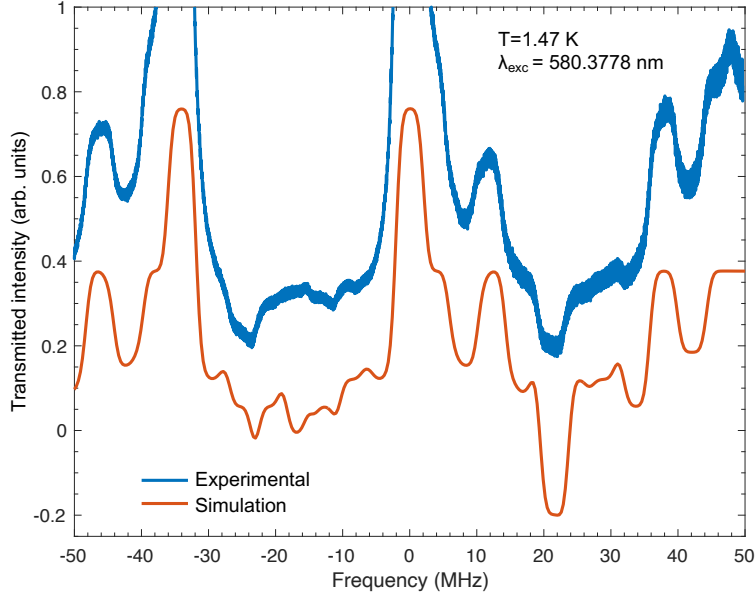


Figure S11: Nuclear spin population transfer to a single level by optical pumping. All-optical spin initialisation to the lowest ground-state nuclear spin level ($\pm 1/2_g$) for an ion ensemble of 3 MHz spectral width in the isotopically enriched Eu^{3+} complex. The experimental spectrum shows good agreement with the simulation for 21.5 MHz and 34 MHz energy splittings in the ground state.

the figure, showing good agreement with the experimental one.

4 AFC and controlled interactions experiments

The AFC protocol is based on a spectral structure of periodic absorbing teeth characterized by a width γ and a separation Δ . An input pulse in resonance with the AFC structure will create superposition states for ions in the teeth, which will rephase and create echoes or output pulses at times $t_k = k/\Delta$ ($k = 1, \dots, N$). This protocol enables very low output noise in the form of spontaneous fluorescence as excited state population is kept very low between input and output pulses. It is moreover well adapted to time or frequency multiplexed memories, which is a very important asset in the context of long distance quantum communications.

The full AFC preparation and storage sequence is displayed in **Fig. S12A**. We first increased

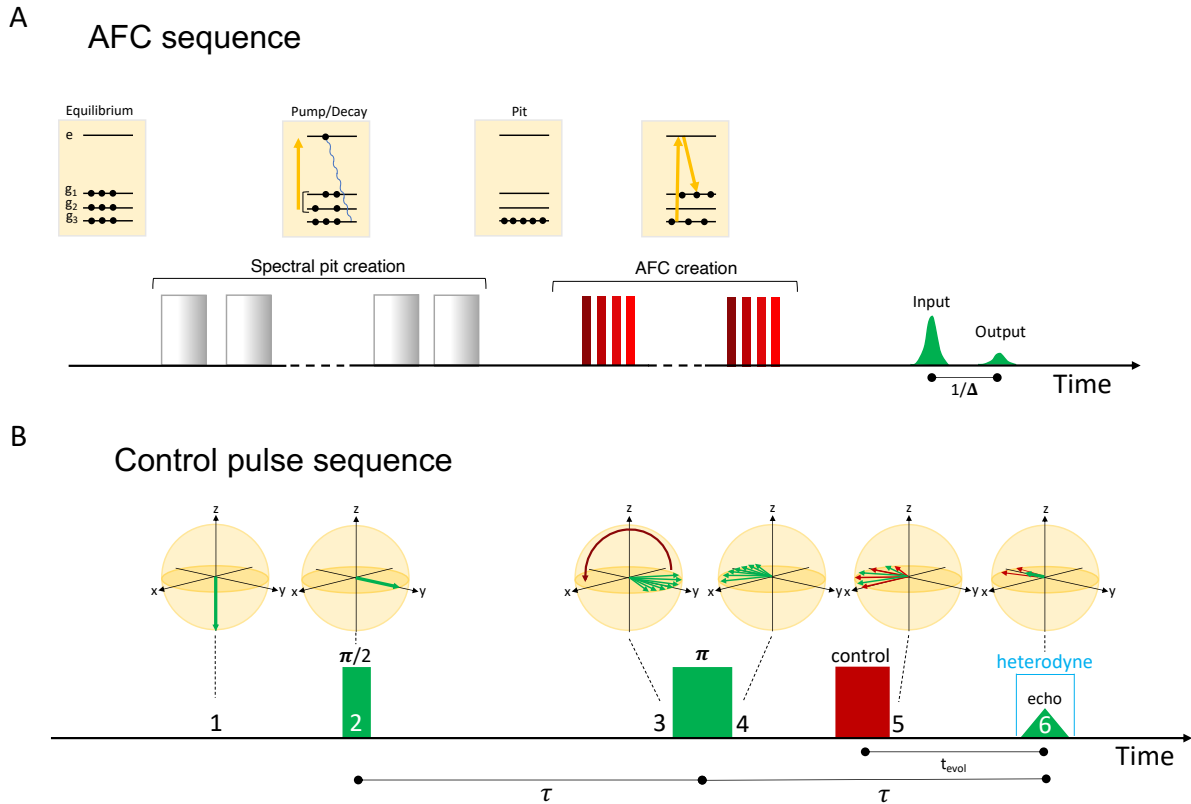


Figure S12: Atomic frequency comb storage sequence and Eu^{3+} - Eu^{3+} interaction control sequence. **A:** The AFC sequence is divided in three steps. First, we create a 9 MHz width spectral pit at frequency 30 MHz, which creates an increased absorption region at 0 MHz detuning. Secondly, a periodic spectral structure is created by SHB in the increased absorption region (AFC). Finally, a weak storage pulse is sent overlapping the AFC, and giving rise to echo emission at delay $1/\Delta$. **B:** Eu^{3+} - Eu^{3+} interaction control sequence. A frequency detuned pulse at -20 MHz (control pulse) is applied between the π pulse and the echo in a 2-pulse echo sequence. This results in reduced echo emission due to increased Γ_h by electric dipole interaction between control and target Eu^{3+} ions.

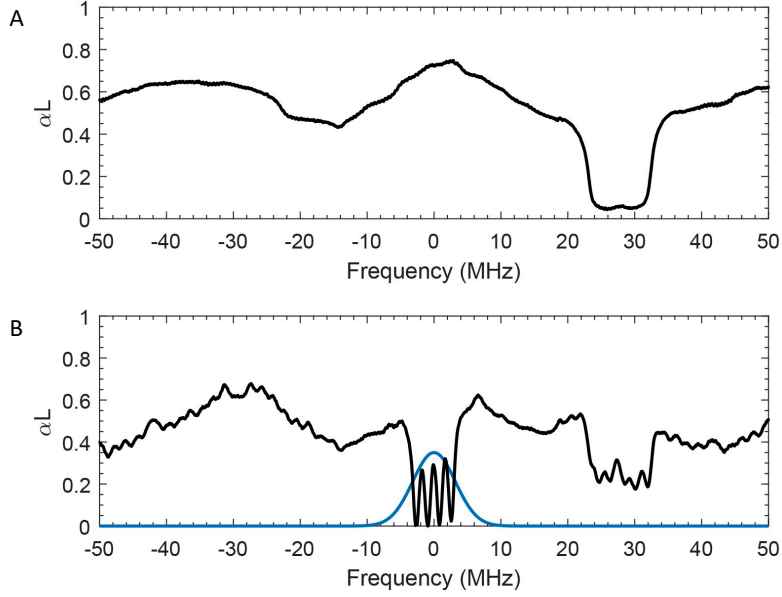


Figure S13: Spectral tailoring prior to AFC storage. **A:** Spectral pit of 9 MHz dug in the absorption profile at 30 MHz to create a high absorption region at 0 MHz. **B:** Atomic frequency comb (AFC) with teeth of 0.9 MHz separated by 1.75 MHz ($F=1.9$). The FFT of the storage pulse is presented over the AFC (blue line), showing good overlap. The input pulse intensity was estimated by sending it through the spectral pit in (**A**), taking advantage of the pit's almost full transparency. A correction was made to account for residual absorption.

population in a spectral region of about 9 MHz by burning a corresponding broad hole (spectral pit) about 30 MHz away (**Fig. S13A**). In a second step, population was burned away at regularly spaced frequencies in the high absorbing region. After optimization of the whole sequence, we succeeded in creating an AFC spanning 6 MHz range with teeth width of 0.9 MHz and 1.75 MHz separation (**Fig. S13B**). This experiment was performed 4.3 GHz away from the transition peak at 580.370 nm (**Fig. S6**) to reduce absorption and facilitate optical pumping. The input pulse intensity for the AFC efficiency estimation was measured through the spectral pit and corrected from remaining residual absorption (**Fig. S13A**).

The AFC storage efficiency in forward mode is given by:

$$\eta_{AFC} = (\alpha L / F)^2 \exp(-\alpha L / F) \exp(-7 / F^2) \quad (4)$$

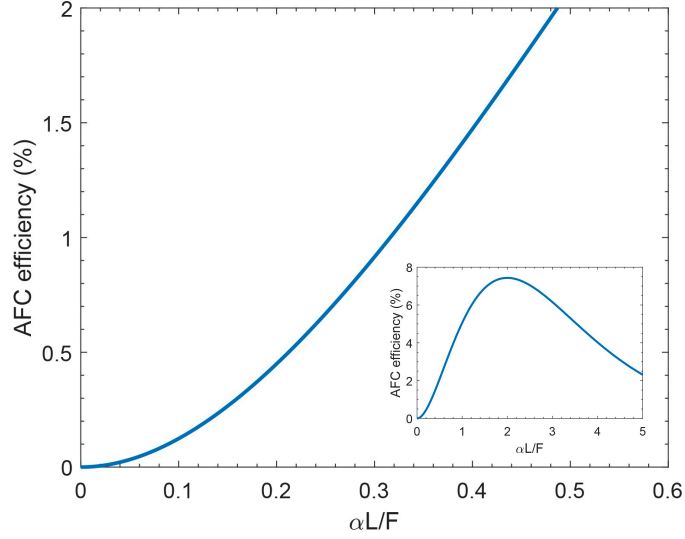


Figure S14: Theoretical efficiency analysis. AFC efficiency as a function of $\alpha L/F$. Inset: AFC efficiency as a function of $\alpha L/F$ showing the maximum achievable efficiency ($\sim 7.5\%$) with an AFC Finesse of 1.9.

where F is the AFC Finesse defined as the teeth width (γ) over teeth separation Δ . The theoretical efficiency curve as a function of $\alpha L/F$ is given in **Fig. S14**. From the intensity ratio between the input pulse and the transmitted pulse through the AFC and effective absorption $\alpha L/F$ of 0.4 is obtained, corresponding to a theoretical AFC efficiency of 1.4% in quite good agreement with the experimental efficiency of 0.86%. The mismatch between theory and experiment could be explained by residual absorption of the storage pulse by ions which do not take part in the AFC (as for instance ions sitting on the sides of the comb region).

Controlled interactions experiments are based on Eu^{3+} permanent electric dipole moments. The frequency shift of a target ion transition when a nearby control ion is excited is given by [11]:

$$\Delta f(r) = \frac{\Delta\mu_{\text{eff}}^2}{h4\pi\epsilon\epsilon_0 r^3} \Theta, \quad (5)$$

where r is the distance between the control and target ions, $\Delta\mu_{\text{eff}}$ the effective dipole moment difference between ground and excited states, ϵ_0 and ϵ , the vacuum permittivity and material

dielectric constant, and Θ a geometric factor depending on the dipole moments and inter-ion vector relative orientations. Taking into account the random spatial distribution of control and target ions, the line broadening of target ions induced by exciting control ions is approximated as [12]:

$$\Gamma_c = (2/3)\pi^2 \frac{\Delta\mu_{\text{eff}}^2}{h4\pi\epsilon\epsilon_0} \rho_0 p, \quad (6)$$

where ρ_0 is the control ion density and p the fraction of excited control ions. Note that the expression given in the main text for the target ion echo amplitude decay as a function of the evolution time t_{evol} takes into account that excited control ions do not decay during the echo sequence, i.e. $T_1 \gg t_{\text{evol}}$.

The excitation induced frequency shift is also present in the 2 pulse PE experiment as the rephasing pulse exchanges ground and excited state populations, an effect known as instantaneous spectral diffusion (ISD) [13]. The experimental value $\Gamma_c = 14.5$ kHz gives an upper bound to the ISD contribution as ions in the PE sequence are already excited by the first pulse.

At the smallest distance between Eu^{3+} ions in the molecular crystal, $r_0 = 0.9886$ nm, we estimate a maximal frequency shift of $\Delta f(r_0) = 85.6$ MHz, extrapolated from $\Delta\mu_{\text{eff}} = 50$ kHz/(V/cm) in $\text{Eu}^{3+}:\text{Y}_2\text{O}_3$ and $\epsilon_{\text{Y}_2\text{O}_3} = 15$ [14] and assuming a refractive index $n = 1.5$ for the molecular crystal and thus $\epsilon = n^2 = 2.25$ [15]. From the experimental value $\Gamma_c = 14.5$ kHz, we then deduce $p = 8.2 \times 10^{-8}$ or 8×10^{13} ions/cm³, a value consistent with typical photon echo experiments (13). The estimation of $\Delta f(r_0)$ also gives the number of target ions around a control ion for which the frequency shift is larger than the homogeneous linewidth. With $\Gamma_h = 30$ kHz, this corresponds to a sphere of radius 13.7 nm containing about 10000 target ions.

Supplementary references

1. C. Brecher, H. Samelson, and A. Lempicki, Laser Phenomena in Europium Chelates. III. Spectroscopic Effects of Chemical Composition and Molecular Structure, *J. Chem. Phys.* 42, 1081 (1965).
2. H. Bauer, J. Blanc, and D.L. Ross, Octacoordinate Chelates of Lanthanides. Two Series of Compounds, *J. Am. Chem. Soc.* 86, 23, 5125–5131 (1964).
3. Marcus O. Workman and John H. Burns, Isomeric forms of some .beta.-diketone complexes of europium(III) and neodymium(III), *Inorg. Chem.* 8, 7, 1542–1544 (1969).
4. L. J. Nugent, M. L. Bhaumik, S. George, and S. M. Lee, Ligand Field Spectra of Some New Laser Chelates, *J. Chem. Phys.* 41, 1305 (1964).
5. A. V. Aristov, Yu. S. Maslyukov, M. I. Gryaznova, G. A. Domrachev, L. A. Aslanov and A. L. Il'inskii, Structure of the tetrakis(benzoylacetonate) compound of europium used to obtain the laser effect, *Theoretical and Experimental Chemistry* volume 6, 53–57 (1972).
6. D. Casanova, M. Llunell, P. Alemany, S. Alvarez, The Rich Stereochemistry of Eight-Vertex Polyhedra: A Continuous Shape Measures Study, *Chemistry A European Journal* 11, 5 (2005).
7. N. Kunkel, J. Bartholomew, S. Welinski, A. Ferrier, A. Ikesue, and P. Goldner, Dephasing mechanisms of optical transitions in rare-earth-doped transparent ceramics, *Phys. Rev. B* 94, 184301 (2016).
8. B. Lauritzen, N. Timoney, N. Gisin, M. Afzelius, H. de Riedmatten, Y. Sun, R. M. Macfarlane, and R. L. Cone, Spectroscopic investigations of $\text{Eu}^{3+}:\text{Y}_2\text{SiO}_5$. *Phys. Rev. B* 85, 115111 (2012)..

9. A. J. Silversmith and N. B. Manson, Determination of the ^{153}Eu - ^{151}Eu quadrupole-moment ratio by excited-state optically detected nuclear magnetic resonance, *Phys. Rev. B* 34, 4854 (1986)..
10. M. Macfarlane, A. Arcangeli, A. Ferrier and P. Goldner, Optical Measurement of the Effect of Electric Fields on the Nuclear Spin Coherence of Rare-Earth Ions in Solids, *Phys. Rev. B* 113, 157603 (2014)..
11. R. Ahlefeldt, D. L. McAuslan, J. J. Longdell, N. B. Manson, and M. J. Sellars, Precision Measurement of Electronic Ion-Ion Interactions between Neighboring Eu^{3+} Optical Centers, *Phys. Rev. Lett.* 111, 240501 (2013)..
12. S. B. Altner, M. Mitsunaga, G. Zumofen, and U. P. Wild, Dephasing-Rephasing Balancing in Photon Echoes by Excitation Induced Frequency Shifts, *Phys. Rev. Lett.* 76, 1747 (1996).
13. F. Könz, Y. Sun, C. W. Thiel, R. L. Cone, R. Equall, R. Hutcheson, and R. M. Macfarlane, Temperature and Concentration Dependence of Optical Dephasing, Spectral-Hole Lifetime, and Anisotropic Absorption in $\text{Eu}^{3+}:\text{Y}_2\text{SiO}_5$, *Phys. Rev. B* 68, 085109 (2003).
14. A. Fossati, S. Liu, J. Karlsson, A. Ikesue, A. Tallaire, A. Ferrier, D. Serrano, and P. Goldner, A Frequency-Multiplexed Coherent Electro-Optic Memory in Rare Earth Doped Nanoparticles, *Nano Lett.* 20, 7087 (2020).
15. R. M. Macfarlane, Optical Stark Spectroscopy of Solids, *J. Lumin.* 125, 156 (2007).